APPLIED SCIENCES AND ENGINEERING

Formation of discrete periodic nanolayered coatings through tailoring of nanointerfaces—Toward zero macroscale wear

Mahdi Khadem[1,2], Oleksiy V. Penkov[3], Jibi Jais[4], Su-Min Bae[5], Vishnu Shankar Dhandapani[6], Bongchul Kang[4], Dae-Eun Kim[1,2]*

Notwithstanding the success of nanolayered coatings in the reduction of wear at nano-/microscales, the improvement of the wear resistance at the macroscale remains an issue. Moreover, the effects of nanointerfaces in nanolayered coatings on their macrotribological properties are not understood well. This paper reports on the engineering of nanointerfaces in diamond-like C/Cr nanolayered coatings to tailor their characteristics including the degree of intermixing, defects, and Cr growth mode. The result was the fabrication of a coating with subnanometer-thick periodic albeit discrete Cr interlayers. This was achieved using our patented deposition technique. This coating contained less interfacial defects compared to classic nanolayered coatings with continuous nanolayers and presented record-breaking wear rates at the macroscale. Finite Element analysis was performed and micropatterning strategy was used to reduce the wear rate further. Last, we report on discovery of a dimensionless parameter that can be used to predict the wear resistance of carbon-based nanolayered coatings.

INTRODUCTION

The loss sustained by industries because of the degradation in efficiency associated with friction and wear phenomena accounts for 23% of the world's total energy consumption (*1*, *2*). In three major sectors of energy, transportation, and residential, the energy required to compensate wear-related failures are 24, 33, and 12% of the total energy consumed, respectively (*1*). These alarming statistics persuaded researchers and scientists to actively identify effective strategies to reduce friction and wear. By date, application of lubricants and surface modification techniques has been introduced as the potential solutions. Among the surface modification techniques, the deposition of functional multilayer coatings and surface patterning have been demonstrated to be highly effective (*3*, *4*). The capability to manipulate compressive residual stress, shear strength, crack propagation, and elasticity through strategic stacking of coating layers in a multilayer coating is particularly effective for reducing friction and wear (*5*, *6*).

Key parameters including the order and thickness of individual layers and properties of the material used for individual layers [e.g., hardness (*H*), elastic modulus (*E*), chemical compatibility, etc.] should be considered while designing a multilayer functional coating for tribological applications (*5*). While selecting the materials, three essential criteria must be satisfied: First, the selected materials should be capable of maintaining an amorphous state during deposition. An amorphous state is desirable because such structures exhibit higher elasticity compared with their polycrystalline counterparts. Essentially, the concept is to absorb the contact energy through an elastic rather than plastic process during the sliding test (*6*). Second, the intermixing of the materials should be limited. Otherwise, a layered structure with distinct boundaries cannot be formed. Last, the materials should inherently display low friction and wear properties.

Although the abovementioned criteria are acknowledged by researchers, there is another criterion that its effect on determining the friction and wear properties of nanolayered coatings has been undermined by date: the effect of nanointerfaces including growth mode of the nanolayers during deposition, interfacial defects, and the degree of intermixing. In general, the coatings grow epitaxially according to three primary modes (*7*): Volmer-Weber [VW; three-dimensional (3D) island growth], Stranski-Krastanov (SK; layer plus island growth), and Frank–van der Merwe (FM; 2D layer-by-layer growth). The properties of the coatings (particularly in the case of nanolayered coatings with many interfaces) can be altered markedly because each of these growth modes has unique characteristics at the atomic level. Growth in the VW mode results in a higher degree of crystallinity and large crystal size. This, in turn, results in defective rough interfaces in nanolayered coatings (*8*, *9*). On the other hand, in the FM growth mode, the 2D nuclei that are formed subsequently coalesce on atomically flat terraces because of the high supersaturation of the film precursors (*10*). SK growth is an intermediate mode that can be characterized by both 2D layer and 3D island growths. In this mode, the system of uniform thickness is thermodynamically unstable, resulting in inhomogeneous regions, some very thick and some completely uncovered.

FM growth is the most desirable growth mode because of the feasibility of atomic-scale control of the layer thickness and interfacial structure (*10*). This results in the formation of dense and atomically smooth interfaces with the minimum intermixing and structural defects (*8*, *11*, *12*). This is particularly desirable in the coatings for optical applications in which the formation of smooth and low defective interfaces is critical (*13*). With regard to the mechanical properties, amorphous coatings grown in the FM mode exhibited a higher elastic response (*H*/*E* ratio) than those of coatings grown in the SK or VW mode (*14*, *15*). In sputtering, FM growth can be

[1]Department of Mechanical Engineering, Yonsei University, Seoul 03722, Korea. [2]Tribology Research Lab, Yonsei University, Seoul 03722, Korea. [3]ZJU-UIUC Institute, Zhejiang University, Haining, Zhejiang 314400, China. [4]School of Mechanical Engineering, Kookmin University, Seoul 02707, Korea. [5]Department of Mechanical Engineering, University of Tokyo, Tokyo 113-8656, Japan. [6]PG & Research Department of Physics, PSG College of Arts & Science, Coimbatore, 641014 Tamil Nadu, India.
*Corresponding author. Email: kimde@yonsei.ac.kr

achieved at low deposition pressure and temperature (*10*, *14*). However, it is difficult to maintain the FM coating growth because this mode is exceptionally sensitive to the physical properties that are linked to the deposition parameters. Previous studies have reported that the growth mode may switch by manipulating the deposition power and therefore the corresponding changes in deposition rate, kinetic energy of the adatoms, and even temperature at atomic level (*16*–*18*). An increase in the deposition pressure during sputtering resulted in a transition of the growth mode from FM to SK and VW (*14*, *15*). In addition, a transition from FM to SK may occur at a critical thickness during coating deposition (*19*–*21*). This discussion implies that transition of the growth mode during the deposition of nanolayered coatings can markedly alter the nanostructural, mechanical, and therefore tribological characteristics. Hence, coating materials that preferably grow according to FM mode must be selected to construct periodic nanolayered coatings for tribological applications.

In a recent study (*3*), the effects of nanoscale interfaces (intermixing) on the friction and wear properties of C/SiN nanolayered coatings at the nano-/microscales under low load (range of millinewton) were investigated. It was observed that by tuning the energy of the arriving C atoms/ions, the intermixing properties could be tailored, and thereby, the tribological properties could be altered significantly. However, the effects of interfacial defects and changes in the growth mode associated with the tuning of the energy of carbon ions/atoms on the friction and wear properties remain undiscussed. Moreover, the effects of nanoscale interfaces on macroscale wear remains unclear. Last, it should also be noted that despite significant advances in the reduction of wear at the nano- and microscales, overcoming of wear at the macroscale remains a challenging task.

The discussed criteria in materials selection for the fabrication of a nanolayered structure narrows down the number of candidates. Diamond-like carbon (DLC) is one of the potential candidates with attractive mechanical and tribological properties that satisfy the requirements and is used in a majority of multilayer functional coatings. A shortcoming of DLC is the high level of internal stress. This limits the coating thickness and, thereby, may exert negative effects on the wear properties (*5*). Low adhesion to metal substrates is another shortcoming of DLC. To overcome these shortcomings, many researchers have used metallic interlayers in combination with DLC (*5*, *22*). The interlayers have an important role in the stress release mechanism and in decreasing the stress discontinuity at the interface between adjacent layers (*23*). Cr is used frequently in carbon-based systems either as a sublayer (strong adhesion to steel materials) or an interlayer (because it displays zero or low intermixing with carbon) (*24*). According to a previous study, Cr can potentially grow in FM mode when combined with carbon (*25*). This enables the formation of atomically thick, continuous Cr layers in a DLC medium, which is essential for the design of nanolayered coatings as discussed earlier.

Considering the mechanisms and advantages explained above, DLC and Cr were selected to construct the nanolayered coatings in this study. The coatings were deposited onto high-speed steel (HSS) substrates. The interfacial properties including the degree of intermixing at nanoscale interfaces and growth mode of Cr nanolayers were tailored to investigate their effects on the friction properties and wear resistance and to optimize the coatings with regard to these parameters. This was achieved using our patented deposition technique, as follows (*26*): DLC and Cr nanolayers were sequentially deposited at the fixed times of 100 and 4 s, respectively. The deposition power remained constant for DLC, whereas the Cr deposition power (magnetron power) was varied from 20 to 150 W (20, 40, 80, 120, and 150). Variation of the thickness of metallic nanolayers using our method has particular advantages. The degree of crystallinity in metallic nanolayers (in this case, Cr) is lower and the cluster sizes are smaller than those of DLC/metallic-based nanolayered coatings prepared by other methods (*27*, *28*). For clarity, the specimens were denoted as Cr150, Cr120, Cr80, Cr40, and Cr20 based on their respective Cr deposition powers. A coating composed of a Cr sublayer and DLC layer (henceforth denoted as DLC coating) was also prepared for comparison.

Our comprehensive analysis revealed that manipulation of the deposition power of Cr nanolayers substantially affects the degree of DLC/Cr intermixing, nature and quantity of the interfacial defects, and the growth mode of Cr nanolayers. The transition of growth mode exerted a significant effect on the macrotribological properties. By engineering the nanointerfaces, a new class of nanolayered coatings for tribological applications in which the nanostructure is periodic but the nanolayers are discontinuous (discrete) was fabricated. This coating not only showed all the features of those of classic nanolayered coatings (in which the nanolayers are continuous) but also contained less interfacial defects because of the discrete form of the Cr nanolayers. According to our benchmarks, despite having a lower thickness, the coating displayed a lower coefficient of friction (COF) and a record-breaking wear rate at the macroscale. Our observations implied that an additional criterion, which is growth of coating materials according to early stages of FM mode, must be considered and added to those of conventional criteria to construct nanolayered coatings for macrotribological applications. We also report the identification of a dimensionless parameter that can be used to explain and predict the macroscale wear behavior of the carbon-based nanolayered coatings. Finite Element (FE) simulations were performed to analytically investigate the state of the induced stresses in the substrate before and after deposition of the coatings upon contact and sliding. Last, to further reduce the wear rate of the coating with the highest wear resistance, surface micropatterning strategy along with lubrication was used. A comprehensive model to describe and predict the macroscale wear in this scenario based on those of acknowledged governing mechanisms was proposed.

RESULTS

Tailoring of the nanointerfaces: Growth mode and intermixing

Figure 1 (A to D) shows high-resolution transmission electron microscopy (HR-TEM) images and 3D-rendered schematics of morphology of the nanointerfaces of Cr40, Cr80, Cr120, and Cr150 coatings, respectively (Cr20 coating is discussed separately in Fig. 2). The thicknesses of the Cr sublayer and individual DLC layers were fixed at approximately 60 and 5 nm, respectively, and were uniform for all the coatings. The resulting overall thickness of the coatings based on the deposition conditions was ~520 ± 30 nm. Magnified HR-TEM images revealed the significant effects of the Cr deposition power on the DLC/Cr nanointerfaces and growth mode of Cr nanolayers. The DLC nanolayers displayed and maintained a fully amorphous nanostructure. In the case of Cr40, the Cr

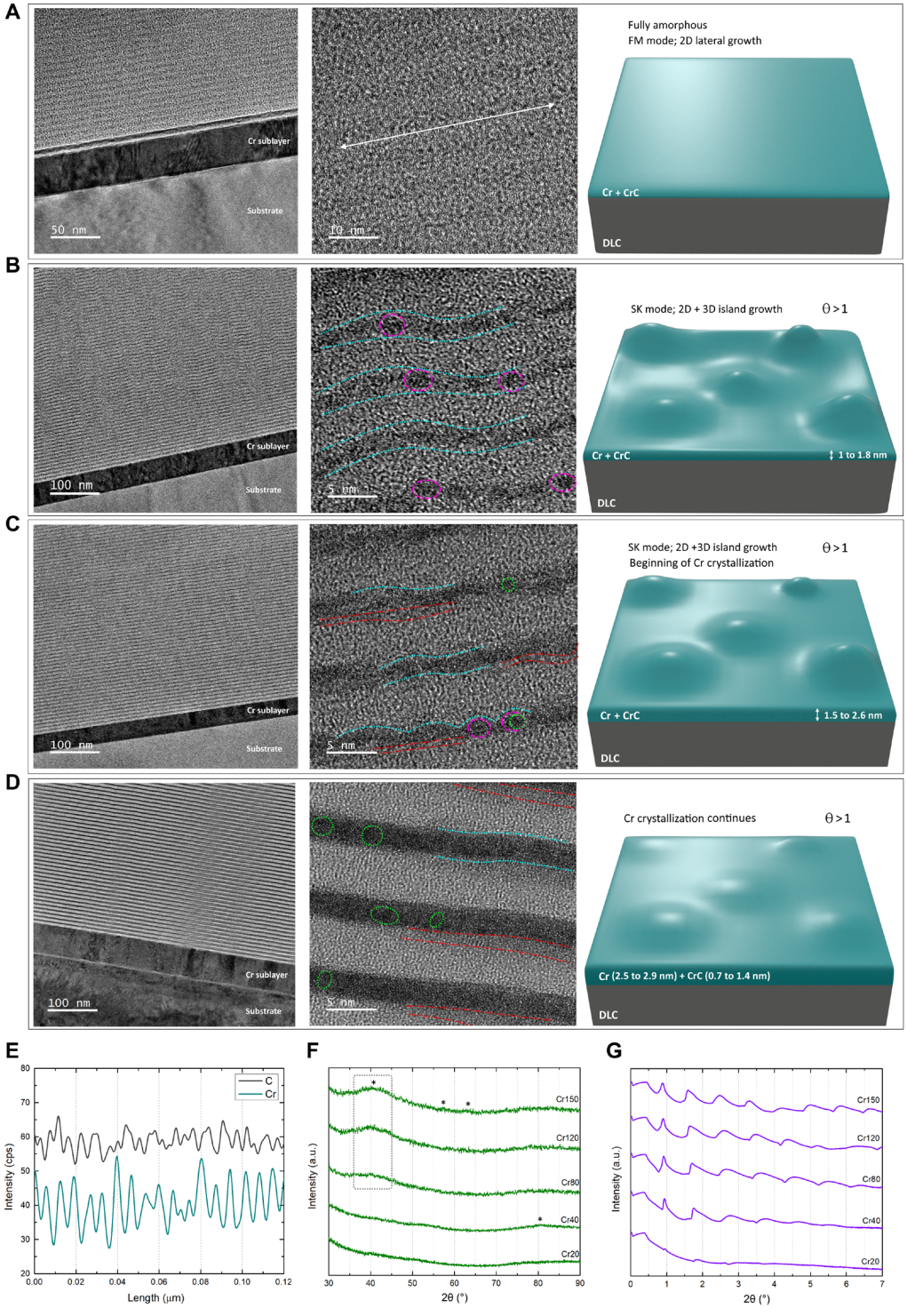

Fig. 1. The effects of Cr deposition power on the nanostructure and intermixing. High-resolution transmission electron microscopy (HR-TEM) images of the deposited nanolayered coatings and 3D schematics of the morphology of individual Cr-DLC nanointerfaces: (**A**) Cr40, 2D lateral growth (FM mode) of Cr nanolayers on DLC along the arrowed white line. (**B**) Cr80, transition of growth mode from FM to SK (2D + 3D island). Certain islands are marked with pink circles. A few of the wavy and rough interfaces are specified with blue dashed lines. (**C**) Cr120, the islands continue to grow and coalesce in the SK mode. A higher degree of intermixing occurs. Cr begins to crystallize. The intermixed layers and nanocrystalline phases are specified with red dashed lines and green circles, respectively. (**D**) Cr150, crystallization of Cr continues. A few of the nanocrystalline phases are circled by green dashed lines. (**E**) Line energy-dispersive spectroscopy (EDS) analysis of the Cr120 coating. (**F**) X-ray diffraction (XRD) analysis (2θ, 30° to 90°) of the nanolayered coatings. Features that were detected at 41°, 56°, 64° and 80° are marked with *. a.u., arbitrary units. (**G**) LAXRD analysis (2θ, 0° to 7°) of the nanolayered coatings. The surface coverage area is denoted by Θ.

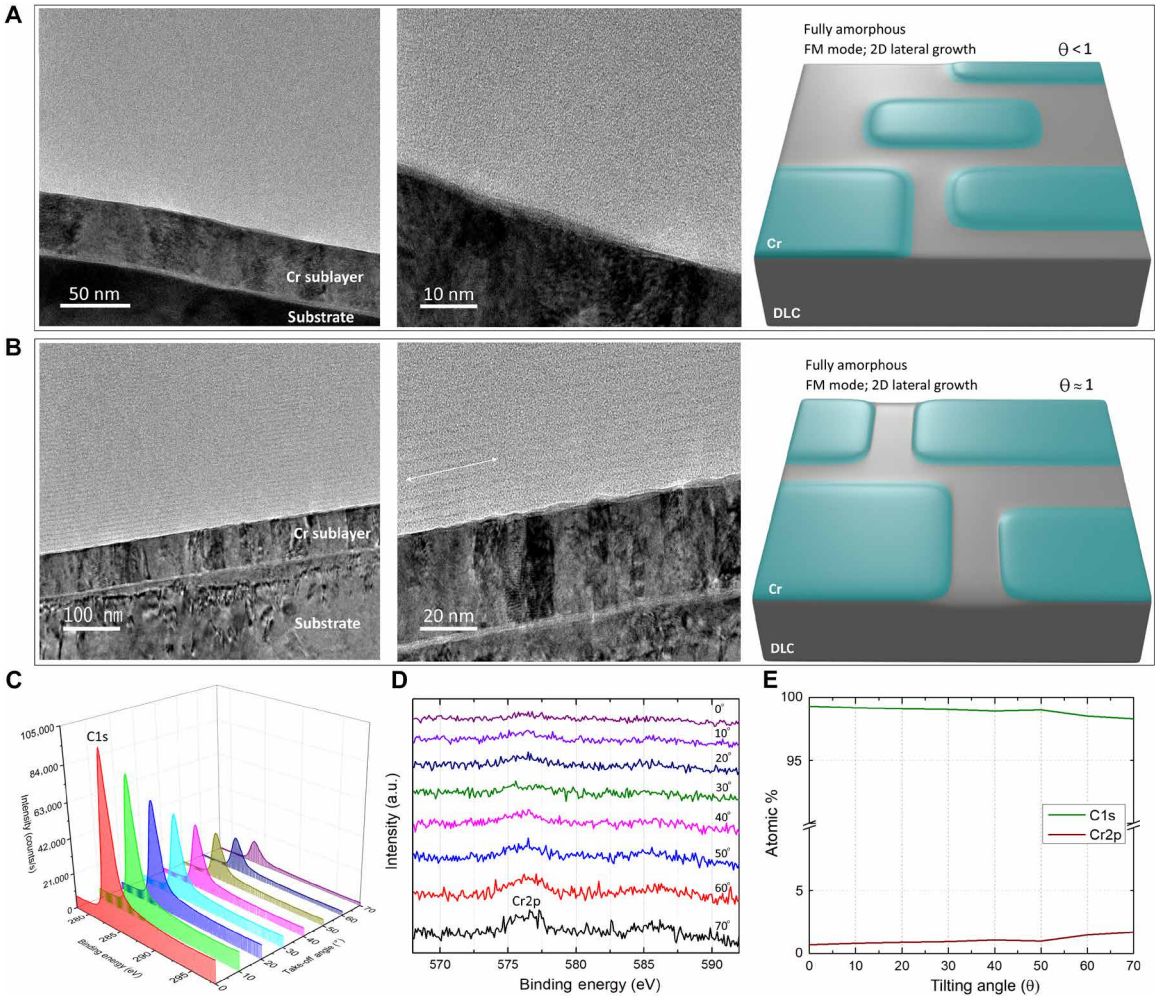

Fig. 2. Analysis of nanointerfaces and Cr growth mode in Cr20 coating. HR-TEM images of Cr20 coating with Cr deposited for (**A**) 4 s and (**B**) 10 s. A 2D lateral growth (FM mode) of Cr nanolayers on DLC can be observed along the arrowed white line. The 3D-rendered schematics show the state and morphology of the individual Cr-DLC nanointerfaces at different stages of Cr growth in the FM mode. (**C** and **D**) AR-XPS analysis for Cr20 coating (take-off angle, 0° to 70°; step, 10°). Variations in the intensity of $C1_s$ and $Cr2_p$ peaks with respect to the take-off angle. (**E**) The atomic % of C showed a decrease as the take-off angle varied from 0° to 70°. Meanwhile, the atomic % of Cr increased, indicating the presence of atomically thin discrete Cr nanolayers in the DLC medium. The surface coverage area is denoted by Θ.

nanolayers showed a tendency to grow laterally (in plane; 2D) and follow the amorphous nanostructure of the underlying DLC layer. Moreover, the nanointerfaces were highly smooth. These characteristics are representative of growth in the FM mode. The contrast between individual DLC and Cr nanolayers was low because of the low density and thickness of the Cr nanolayers. The low contrast can also be attributed to a certain degree of intermixing. Owing to these phenomena, an accurate measurement of the thickness of Cr nanolayers was not possible. An increase in the Cr deposition power from 40 to 80 W resulted in an evident transition in the growth mode of individual Cr nanolayers from FM to SK. The islands started to form as the thickness of the Cr nanolayers exceeded a critical limit of ~1.1 nm. At this stage, the growth occurred mainly through the nucleation and coalescence of adsorbate islands. The contrast between DLC and Cr nanolayers was observed to be higher than that for Cr40. The formation of random Cr islands within the intermixed phase resulted in rough and wavy nanointerfaces (this matter is discussed further in a subsequent section) wherein the thickness of Cr nanolayers was nonuniform (~1 to ~1.8 nm including the intermixed phase). The islands continued to grow in the SK mode as the Cr deposition power increased from 80 to 120 W. More Cr islands started to form within the intermixed phase and more coalescence took place. The nonuniformity in the thickness of individual Cr nanolayers persisted (~1.5 to ~2.6 nm including the intermixed phase). The contrast between the DLC and Cr nanolayers and the level of intermixing at the interfaces increased. A closer inspection of the Cr nanolayers in this coating revealed the presence of nanocrystals enveloped in the surrounding amorphous phase. The contrast between the DLC and Cr continued to increase as the Cr deposition power increased to 150 W. Individual DLC and Cr layers were distinctly visible in Cr150 coating. A definite boundary between Cr and the intermixed layers was recognizable. The thickness of the individual Cr layers became more uniform as more islands coalescence (Cr, ~2.5 to ~2.9 nm; intermixed layer, ~0.7 to ~1.4 nm). The quantity and size of the nanocrystalline phases increased compared to Cr120 coating and was in the range of ~1.1 to ~1.6 nm.

The degree of intermixing at the interfaces of the DLC and Cr nanolayers was observed to be higher than that for the other nanolayered coatings.

Figure 1E presents the energy-dispersive spectroscopy (EDS) analysis of the Cr120 coating extracted from a section of the nanolayered region. Alternation of C and Cr is evident. This verifies the periodic presence of the elements as intended. Figure 1F presents the x-ray diffraction (XRD) patterns of the coatings. The diffractograms of the Cr150, Cr120, and Cr80 coatings show broad features at 2θ ~41°, which indicate the amorphous characteristic of the intermixed regions (*28*). In the case of the Cr150 coating, additional less-intense features are observed at 2θ ~56° and 64°. The first two peaks at 41° and 56° can be attributed to a metastable phase of chromium carbide (CrC_x) with NaCl structure that can be observed in sputtered Cr-C coatings (*29*, *30*). The other weak feature in this coating at 2θ ~64° can be assigned to the Cr (200) plane (*31*). This feature was also detected for Cr120 coating. The intensity of the peaks decreased, and the latter features disappeared as the Cr deposition power decreased from 150 to 80 W. All the abovementioned features disappeared when the power was reduced to 40 W. Rather, a very weak feature at 2θ ~80° was detected (*28*). Overall, the broad and weak features of the diffractograms imply that the nanostructure of the coatings was mainly amorphous with marginal metastable CrC_x intermixed phases (with the exception of the Cr20 coating, which was fully amorphous and did not show any feature). These results imply that as the Cr deposition power increased from 40 to 150 W, the extent of intermixing that contained amorphous metastable chromium carbide phases increased. The data agree with our observations from HR-TEM imaging.

Low-angle XRD (LAXRD) was used to investigate the effects of the Cr deposition power on nanoscale interfaces more comprehensively (Fig. 1G). Distinct periodic peaks were observed from 0° to 7° in the case of the Cr80, Cr120, and Cr150 coatings. The relative intensity of the peaks decreased significantly in the case of the Cr40 coating. The data imply that the contrast between the C and Cr nanolayers and the density of the Cr nanolayers decreased as the Cr deposition power (and thereby, its thickness) decreased. A direct relationship between the density and thickness of Cr nanolayers has been reported in a previous research as well (*25*). These conclusions can be verified by the HR-TEM analysis also, as discussed earlier. In the case of the Cr20 coating, the peaks are almost completely flattened. This indicates the presence of discrete Cr nanolayers in the DLC medium. These analyses verified that the characteristics of nanoscale interfaces, such as the growth mode and the degree of intermixing during the deposition of nanolayered coatings, can be tailored effectively using our deposition method.

Figure 2A presents the HR-TEM image of the Cr20 coating and the proposed 3D schematic of the nanointerfaces. A fully amorphous nanostructure is observed in which the individual Cr nanolayers in the DLC medium are not clearly distinguishable. A closer observation of the HR-TEM images reveals the presence of periodic albeit discrete Cr nanolayers in the DLC medium. The growth occurred in the lateral direction (in plane; 2D). To verify this conclusion, the deposition time of Cr nanolayers was increased from 4 to 10 s (will be denoted as Cr20-10s henceforth), whereas the other deposition conditions remained unaltered. The discrete Cr nanolayers became clearly visible (Fig. 2B). The outlook of the proposed 3D schematics of the morphology of individual Cr-DLC nanointerfaces resembles the characteristics of the early stages of growth ($\Theta < 1$ for Cr20 and $\Theta \approx 1$ for Cr20-10s) according to the FM mechanism (*11*).

Angle-resolved x-ray photoelectron spectroscopy (AR-XPS) was used to estimate the thickness of discrete Cr nanolayers in the Cr20 coating. To access a DLC-Cr interface, the topmost DLC layer (~5 nm) was removed by ion-etching. The ion-etching and XPS measurements were performed simultaneously in vacuum to avoid oxidation. Figure 2 (C and D) presents the variations in $C1_s$ and $Cr2_p$ peaks with respect to the take-off angles. As can be seen, the intensity of C1s peak decreased, while the intensity of Cr2p continued to increase as the take-off angle varied from 0° to 70°. The corresponding variations in the atomic % of C and Cr with respect to the take-off angle is presented in Fig. 2E. As is evident, the atomic % of C decreased as the take-off angle varied from 0° to 70°. Meanwhile, the atomic % of continued to increase. The above phenomena are assignable to the fact that the depth of data acquisition decreases as the take-off angle increases. These results imply that at least one monolayer that is composed of Cr adatoms/ions (<0.2 nm) was present at the nanointerfaces in a discrete form (as continuous Cr nanolayers were not observed in HR-TEM images).

Determination of chemical and nanostructural properties

Figure 3A shows the Raman spectra of the coatings in the range of 500 to 2000 cm^{-1} (refer to texts S1 and S2 for details regarding the topography, Raman, and XPS analysis of DLC coating). Two distinct peaks are visible in the Raman spectrum of all the coatings. The smaller peak (centered at ~700 cm^{-1}) is considered to be a result of vibrational density of states of sp^2 and/or sp^2-sp^3 hybrids in amorphous carbon (*32*). A few researchers have assigned this peak to the in-plane rotation of sixfold carbon rings (L mode) that corresponds to the phonon density of states of graphite (*33*, *34*). However, the first interpretation is more probable because the peak does not display substantial modifications even when the excitation wavelength is varied (*32*, *35*, *36*).

A closer inspection of the overall Raman spectra reveals that by increasing the Cr deposition power: (i) the intensity of both peaks decreases. This phenomenon can be attributed to the fact that the weight percentage (wt %) of C to Cr in the coating decreases as the Cr deposition power increases, and (ii) the larger peak tends to widen and shift toward higher wavelengths (refer to the pink dashed line in Fig. 3A as the reference line). The Gaussian deconvolution of the larger peak revealed the presence of three subpeaks in all the coatings, known as *I*, *D*, and *G* peaks. According to the previous studies, the first subpeak (denoted as *I* and centered at ~1105 to ~1134 cm^{-1}) can be assigned to either trans-polyacetylene [a strong chain $(C_2H_2)_n$ wherein carbon adopts the sp^2 configuration], C═C stretching and CH wagging modes, or the C─C sp^3 stretching vibration in amorphous carbon phase (*37*–*40*). It is known that Raman cannot be used as a direct method to characterize/quantify the sp^3 bonds. Moreover, the variations in the intensity of this peak with respect to the laser excitation energy are not in compliance with the characteristics of sp^3 sites (*38*).Therefore, it is less likely that this peak originates from the stretching vibration of sp^3 bonds. It should be noted that hydrogen was not incorporated during the deposition process of our coatings. Therefore, we could only attribute the presence of this peak to the absorbance of hydrogen in the atmosphere to the topmost DLC layer before the Raman measurements.

The two main subpeaks (*D* and *G* peaks) are centered in the ranges of ~1369 to ~1388 cm^{-1} and ~1555 to ~1558 cm^{-1}, respectively.

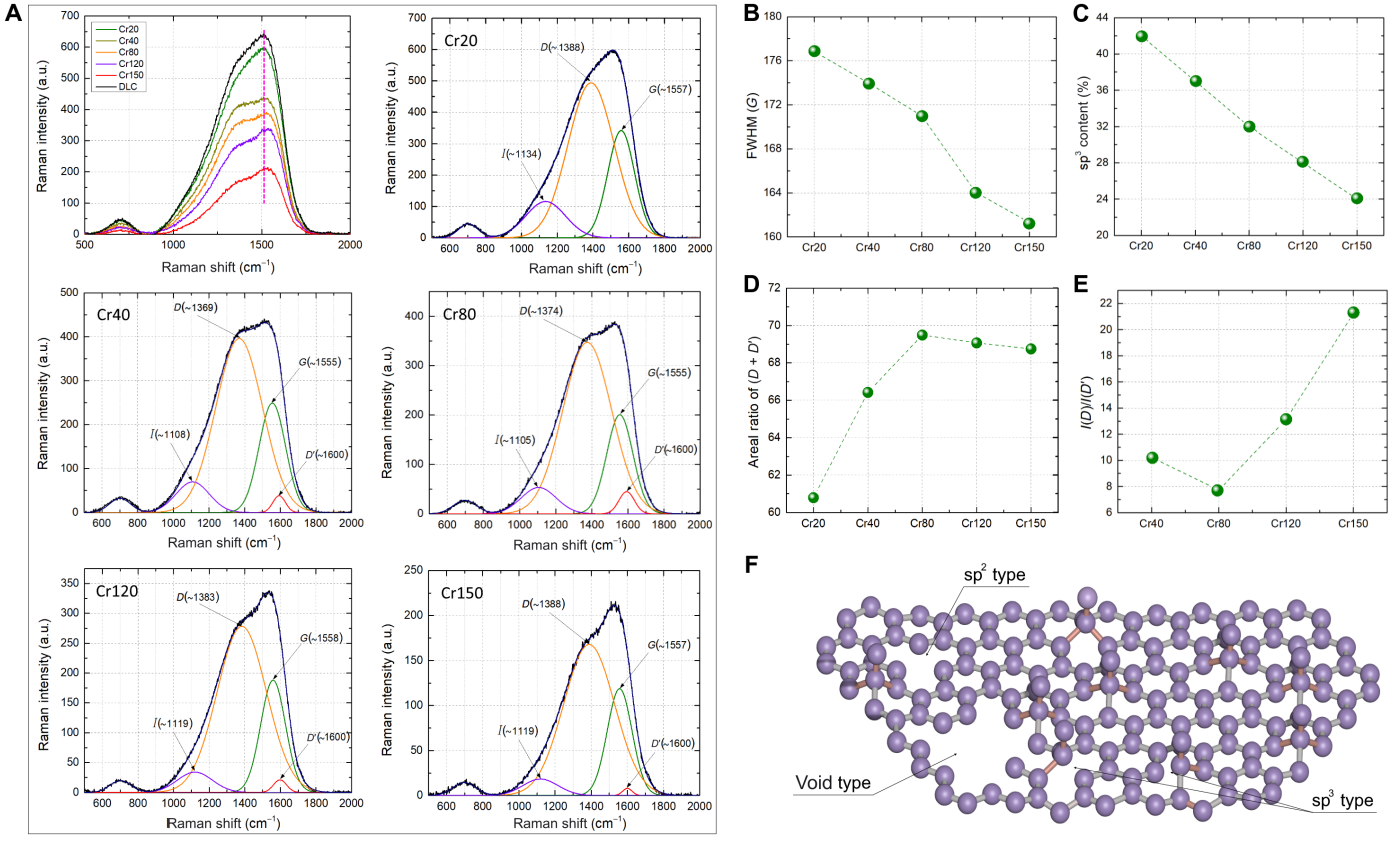

Fig. 3. Nanostructural analysis of the coatings using Raman spectroscopy. (**A**) Overall Raman spectra: The spectra tend to shift (the pink dashed line is the reference) and widen as the Cr deposition power increases. Gaussian deconvolution of the main peak revealed that it consists of four subpeaks known as *I*, *D*, *G*, and *D*′ (≥40 W). Analysis of data obtained from the deconvolutions: variations in (**B**) FWHM(*G*), (**C**) percentage of sp^3 content, (**D**) areal ratio of ($D + D'$), and (**E**) $I(D)/I(D')$ with respect to Cr deposition power. An increase in the Cr deposition power from 20 to 150 W reduces the percentage of sp^3 content from 42 to 24% and alters the quantity and type of nanostructural defects. (**F**) Schematic representation of void, sp^2- and sp^3-type defects in carbon nanostructure.

The *D* and *G* peaks are correlated only with sp^2 sites and can be attributed to breathing and stretching modes, respectively (*41*). An additional peak started to form as the Cr deposition power exceeded 20 W. The formation of this peak (*D*′, centered at ~1600 cm^{-1}) indicates an increase in the concentration of defects and disorders in the amorphous carbon nanostructure as the Cr deposition power increased (*42*, *43*).

The characteristics of the subpeaks were analyzed precisely. Figure 3B shows the variations in the full width at half-maximum (FWHM) of the *G* peak. An evident decrease in the FWHM(*G*) is observed with the increase in the Cr deposition power. The FWHM(*G*) can be used as a parameter to assess the bond length and bond angle distortion in sp^2 clusters that are linked to the sp^3 content in the structure of nonhydrogenated DLC (*44*). With an increase in the sp^3 content, the sp^2 clusters within a sp^3 network become smaller and more strained. This, in turn, causes increases in both bond length and bond angle disorder (*45*). According to Cui *et al.* (*46*), FWHM(*G*) is therefore closely correlated with the sp^3 content in nonhydrogenated DLC, and the concentration of sp^3 bonds can be estimated by this correlation [the sp^3 content increases with the FWHM(*G*) monotonically]. We used this relationship to estimate the percentage of sp^3 content. As shown in Fig. 3C, the percentage of sp^3 content tends to decrease as the Cr deposition power increases. The Cr20 and Cr150 coatings displayed sp^3 contents of 42 and 24%, respectively.

The quantity and type of defects in the coatings was investigated by analysis of the *D* and *D*′ peaks. Figure 3D shows the areal ratio of these peaks [integrated area (*A*) of these peaks divided by the integrated area of all the subpeaks. Note that $A(D') = 0$ for Cr20)]. It is evident that the areal ratio of ($D + D'$) increases as the Cr deposition power increases (from ~61 at 20 W to ~69 at above 80 W). This outcome indicates that the quantity of defects increased significantly as the Cr deposition power increased from 20 to 80 W. The ratio then showed a marginal decrease as the power increased from 80 to 150 W. This can be due to the overall reduction of C wt % as the Cr wt % increases.

Further analysis was performed to investigate the characteristic and origin of the defects in the amorphous carbon structure (Fig. 3E). The ratio $I(D)/I(D')$ can be used to obtain valuable information in this regard (*42*, *47*). It has been reported that $I(D)/I(D')$ is ~13 for sp^3 defects, ~10 for sp^2-related defects, and ~7 for void defects. $I(D)/I(D')$ was observed to be ~10, ~7, ~13, and ~21 for Cr40, Cr80, Cr120, and Cr150, respectively. Note that this analysis is not valid for the Cr20 coating because *D*′ was not observed in its Raman spectrum. Further research is required as it is not clear what the ratio of ~21 signifies. Figure 3F illustrates the defects in the structure of DLC nanolayers.

Effects of nanointerfaces on mechanical properties and internal stress

Figure 4A presents the *H* and *E* values of the coatings measured using a standard diamond Berkovich tip using the Oliver-Pharr method (*48*). These parameters varied in the range of ~13 to ~16 GPa and ~155 to ~190 GPa, respectively. Marginal increases (0.6 to 3 GPa) in the values of *H* (from those for the DLC coating) were detected with the introduction of Cr nanolayers to DLC. Among the nanolayered coatings, *H* and *E* values were influenced by both the amount of sp^3 bonds and formation of CrC_x phases.

The ratio *H*/*E* has also been used widely to assess the mechanical response of thin films under contact as a measure of elasticity (*49*). The variations in *H*/*E* with respect to the Cr deposition power were calculated and are plotted in Fig. 4B. The introduction of the Cr nanolayers to DLC significantly improved its *H*/*E* value. The DLC and Cr20 coatings had the lowest and highest ratio, respectively, among the coatings (0.073 and 0.097, respectively, a difference of 32%). These data indicate that the Cr20 coating had the highest elasticity among the nanolayered coatings. This phenomenon can be attributed to the fact that the Cr20 coating (i) had the least defective nanostructure among the nanolayered coatings, (ii) was fully amorphous, and (iii) contained no carbide phases. The transition of the growth mode from FM to SK and the formation of carbide phases were the causes of the reduction in *H*/*E* with the increase in the Cr deposition power. Considering the overlapping of the standard deviation values in Fig. 4A, we performed a series of statistical analysis (*t* tests) on *H* and *E* values with respect to the claims discussed above. Refer to text S3 for more information.

Figure 4C presents the variations in the accumulated average compressive stress in the coatings. All the nanolayered coatings show a lower internal stress than DLC. These data indicate that the stress was mainly tensile in the Cr nanolayers, while it was compressive in the DLC nanolayers. The tensile stress of layers composed of metallic materials has also been reported in a previous study (*50*). It has also been reported that a higher sputtering power can relieve in-plane compressive stress that enables the formation of layers with a higher degree of crystallinity (*51*). However, the stress did not decrease linearly as the Cr deposition power (and thereby, the thickness of the corresponding Cr nanolayers) increased. Our measurements showed that the stress of the Cr80 coating was higher than that of Cr40. Thus, if we consider the stress of Cr40 as the baseline, the stress became more compressive at 80 W rather than continue being tensile (Fig. 4D). The stress development during coating growth exhibits complex dependences on the conditions during the deposition process (e.g., growth rate and temperature) as well as the coating nanostructure (*50*). The scenario becomes more complex when the coating is in the amorphous state, contains nanocrystals, or is composed of multiple materials (e.g., alloy, composite, and multilayer), wherein phenomenon such as phase transformation is involved. The fundamental mechanisms during coating growth must be considered to address the stress behavior. We discussed previously that the growth mechanism transitions from FM to SK as the Cr deposition power exceeds 40 W. The stress behavior of the Cr80 coating can be explained by this transition and the mechanisms that have been suggested by date. One mechanism suggests that the compressive stress is inherited from the stress in the individual

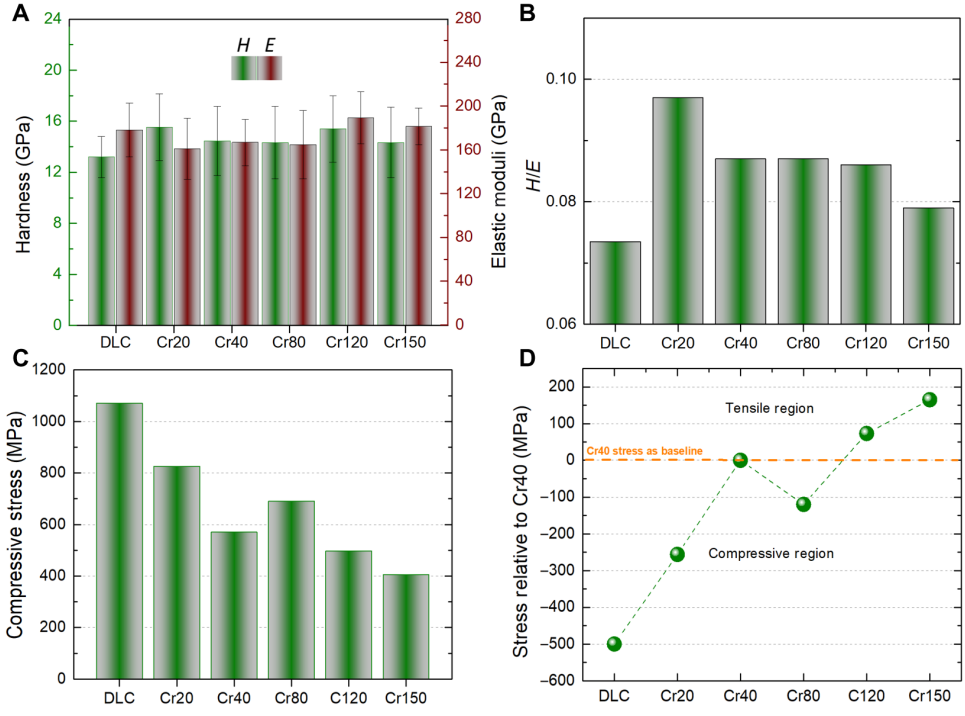

Fig. 4. Nanoindentations and evaluation of internal stress. (**A**) *H* and *E* were measured using a standard diamond Berkovich tip. (**B**) *H*/*E* ratio as a measure of elasticity. Cr20 and DLC show the maximum and minimum *H*/*E* values, respectively. (**C**) Average intrinsic compressive stress of the coatings. The DLC and Cr150 coatings show the maximum and minimum stress (~1070 and ~400 MPa, respectively). (**D**) Evolution of the stress of the coatings relative to that of Cr40 coating. The orange dashed line indicates the zero level as baseline. The regions above (positive) and below (negative) the baseline indicate the tensile and compressive stress regions relative to the stress of Cr40, respectively.

islands before they coalesce, which is attributed to the effect of the surface-induced compressions in the islands before being attached firmly to the underlying surface (*50*). The insertion of atoms to the grain boundaries during the deposition owing to the superposition of atoms on the surface is another proposed mechanism (*52*, *53*). These mechanisms may also be used to explain the formation of rough and wavy nanointerfaces in Cr80 coating. The amount of stress during coating growth can also be correlated with nanostructural defects (*54*); the shrinkage (or closure) of nanoscale defects can be facilitated by compressive residual stress. This indicates that fewer defects are likely at higher compressive stresses, which is in good agreement with the results of the Raman and stress analysis in this study (except for the Cr80 coating because of the explained mechanisms).

Correlations between nanointerfaces and macrotribological properties

Next, the friction and wear behavior of the specimens were assessed. For the initial assessment, the first series of tests were performed under a normal load of 5 N in dry condition. Figure 5A presents the schematic of the custom-built reciprocating macrotribometer. Figure 5B shows the average COF of the specimens for 10,000 cycles. As is evident, the COF of the bare HSS substrate fluctuated over a wide range (~0.4 to ~0.6), which is typical for steel materials. The instability of the COF signal was attributed to the adhesive characteristic of the wear mechanism (see text S4) and severe surface damage. The frictional behavior of the substrate improved significantly after the deposition of coatings. A running-in period of approximately 800 cycles was observed for all the coatings. This is associated with the initial surface roughness. The COFs became steady and stable after the smoothening of micro- and nanoasperities and adaptation of the surfaces in contact as the sliding continued. The DLC and Cr150 coatings showed a similar COF of ~0.1. The COF values for the remaining coatings were in the range of ~0.05 to ~0.08.

After the friction tests, the amount of wear was quantified in terms of normalized wear rate (Fig. 5C). The bare and DLC-coated HSS substrate showed wear rates of 1.7×10^{-9} and 9.8×10^{-11} mm^3/N·mm, respectively. A clear and definite trend between the Cr deposition power and wear rate was observed (the wear rate decreased as the Cr deposition power decreased). The Cr20 coating showed the lowest wear rate (2.1×10^{-11} mm^3/N·mm). The Cr150, Cr120, Cr80, and Cr40 coatings showed wear rates of 4.1×10^{-10}, 2.1×10^{-10}, 1.8×10^{-10}, and 1.6×10^{-10} mm^3/N·mm, respectively. These data imply that the Cr20 coating could effectively reduce the wear of bare HSS by ~81 folds. The data also imply that the wear rates of the Cr150, Cr120, Cr80, and Cr40 coatings were higher than those of the DLC and Cr20 coatings.

Because Cr20 coating showed the lowest wear rate, it was selected for further tests to assess its durability under a higher normal load of 10 N under dry and lubricated conditions. The tests were also performed on bare and DLC-coated HSS specimens for comparison. Figure 5 (D and E) presents the obtained COF data and the wear rates, respectively. The COF of bare HSS continued to fluctuate between 0.5 and 0.6. However, it reduced by ~82% upon the application of Cr20 and DLC coatings, both of which showed a similar COF of ~0.1. Compared with the case of 5 N, the Cr20 coating showed a relatively higher COF of 0.1. This phenomenon can be attributed to the changes in the wear mechanism caused by the increase in the normal load. The obtained wear rates were 2.7×10^{-11}, 1.7×10^{-10}, and 3.8×10^{-9} mm^3/N·mm for Cr20, DLC, and bare HSS, respectively. The Cr20 coating reduced the wear of bare HSS under 10 N by ~140-fold. The wear reduction compared with the only-DLC coating was ~7-fold. An analysis of the wear tracks on the coatings using laser confocal microscopy indicated that abrasive and burnishing wear were the dominant wear mechanisms depending on the Cr deposition power. More specifically, the wear mechanism shifted gradually from burnishing to abrasive as the Cr deposition power increased from 20 to 150 W.

The COF and wear rate reduced significantly under the boundary lubricated condition (Fig. 5, F and G; the lubrication regime is discussed further subsequently). The Cr20 coating exhibited a lower COF (~0.06) than the bare and DLC-coated HSS (~0.082). The bare HSS showed a wear rate of 3.8×10^{-11} mm^3/N·mm, which was significantly lower than that under dry condition. The DLC and Cr20 coatings showed wear rates of 1.4×10^{-11} and 7×10^{-13} mm^3/N·mm, respectively. Figure 5H illustrates a schematic of the abrasive and burnishing wear mechanisms (refer to text S4 for a detailed discussion and to view the wear tracks formed under dry sliding condition). The wear tracks can be seen in Fig. 5I. To summarize, the Cr20 coating was observed to be the optimum coating among the specimens in terms of wear rate. The factors underlying these results are addressed in Discussion.

Evolution and characterization of wear on Cr20 coating

Here, we discuss the wear mechanism of the Cr20 coating more comprehensively. Figure 6A presents a laser confocal microscopy scan of the wear track formed on the Cr20 coating under 5 N. The analysis indicated that the wear mechanism was fully burnishing, because only the micro-/nanoasperities were smoothened out throughout the sliding tests. Another indication of burnishing wear was the nonformation of wear debris alongside the wear track. Moreover, COF generally has a close correlation with R_a in the case of burnishing wear. To investigate this, the surface was monitored by in situ confocal microscopy during the evolution of the wear process. The evolution of the COF and R_a of the worn area with respect to the sliding cycles throughout the test is plotted in Fig. 6B. An evident correlation between COF and R_a is observed. As mentioned earlier, the R_a of the bare HSS substrates was approximately 65 ± 5 nm. Upon the deposition of Cr20 coating, the surface became smoother, and R_a was reduced to 50 ± 5 nm. Both COF and R_a continued to reduce as the sliding test proceeded and then stabilized at 0.08 and ~10 nm, respectively, after ~2000 cycles. The correlation coefficient was calculated to be ~0.98, indicating the presence of a strong dependency between R_a and COF.

The variations in the surface chemistry of the worn area were also investigated by in situ Raman spectroscopy after 50, 500, and 1000 cycles, respectively (Fig. 6, C to E). Table S1 lists the parameters obtained from the Gaussian deconvolutions. No definite trend was observed for the variations in the FWHM(G) with respect to the number of cycles. However, the areal percentages of the G and I peaks [$A(G)$ and $A(I)$] continued to increase and $A(D)$ continued to decrease [whereby $A(D)/A(G)$ decreased] as the number of cycles increased. The increase in $A(I)$ can be attributed to the increase in the number of carbon dangling bonds at the contact interface (*55*), which can readily bond with oxygen during the friction process. The variations in $A(D)$ and $A(G)$ should be explained by considering the $A(D)$ and $A(G)$ values of the as-deposited Cr20 coating. An increase in $A(D)$ during the initial cycles (>500 and <800) can be attributed to an increased disorder in the Cr20 nanostructure.

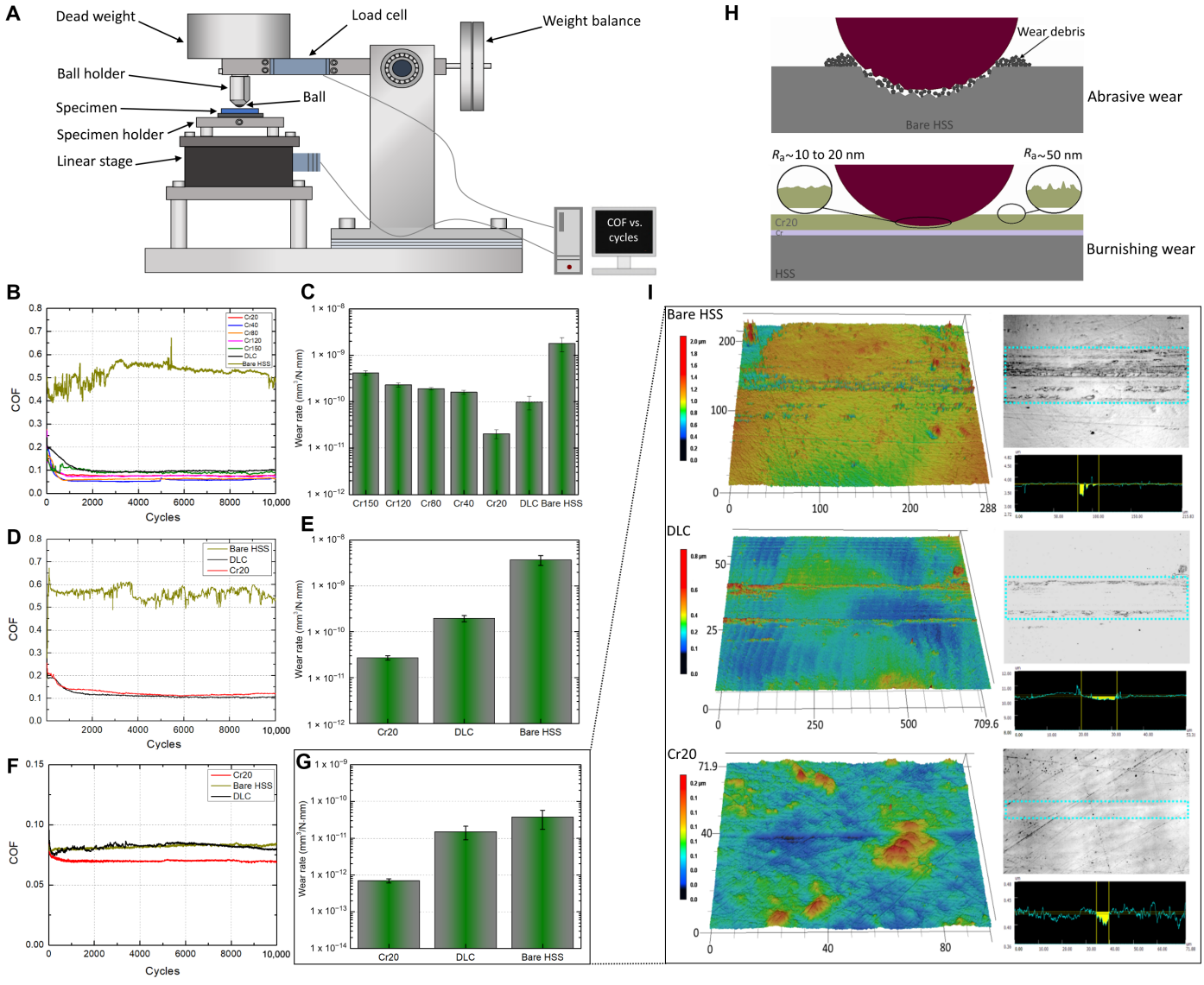

Fig. 5. Evaluation of macrotribological properties. (**A**) Schematic of custom-built reciprocating macrotribometer. Normal loads were applied using standard dead weights. Variations in COF with respect to sliding cycles and wear rate of specimens under dry sliding condition at (**B** and **C**) 5 N and (**D** and **E**) 10 N. (**F** and **G**) Variations in COF and wear rate of bare HSS, DLC, and Cr20 coatings under lubricated sliding condition at 10 N. (**H**) Schematic representation of abrasive and burnishing wear mechanisms. The generation of wear debris and smoothening of micro-/nanoasperities can be observed in the case of each mechanism. (**I**) Visualization of the wear tracks. 3D laser-scanned images, laser-enhanced optical images, and cross-sectional profiles of the wear tracks on bare HSS and on DLC and Cr20 coatings. The areas specified by the yellow color indicate the worn area. The blue dashed lines indicate the boundary of the wear tracks. All the dimensions are in micrometers.

When burnishing wear was involved, the amount of wear during the initial cycles was the highest owing to the rapid leveling of micro-/nanoasperities. This process increased the level of disorder during the initial cycles compared with that for the as-deposited coating. After the leveling/smoothening of the asperities (>800 cycles), $A(G)$ increased, whereas $A(D)$ decreased. This can be an indication of the gradual graphitization of the coating surface owing to the contact pressure and the shear stress generated by friction during the sliding tests (*41*).

FE simulation

FE simulations were performed to assess the state of the induced stress contours during contact and sliding. Cr20 coating was selected as it showed the lowest wear rate among the coatings. Bare and DLC-coated HSS were also simulated for comparison. Plastic behavior was considered for the HSS substrate and the coatings (see texts S3 and S5 for detailed discussion on the procedure used to obtain the plastic properties of the coatings and additional information on the FE modeling, respectively). The ball was only modeled in the elastic mode as it was not the main focus and to reduce the computational time. Refer to the submitted video files to see the evolution of the stress during the contact and sliding actions. Figure 7 (A to C) shows the von Mises stress contours in the substrates at the symmetry plane. The tip and the coatings are hidden in the figures to display the stress contours in the substrates. As it is evident, deposition of DLC and Cr20 coatings onto the HSS

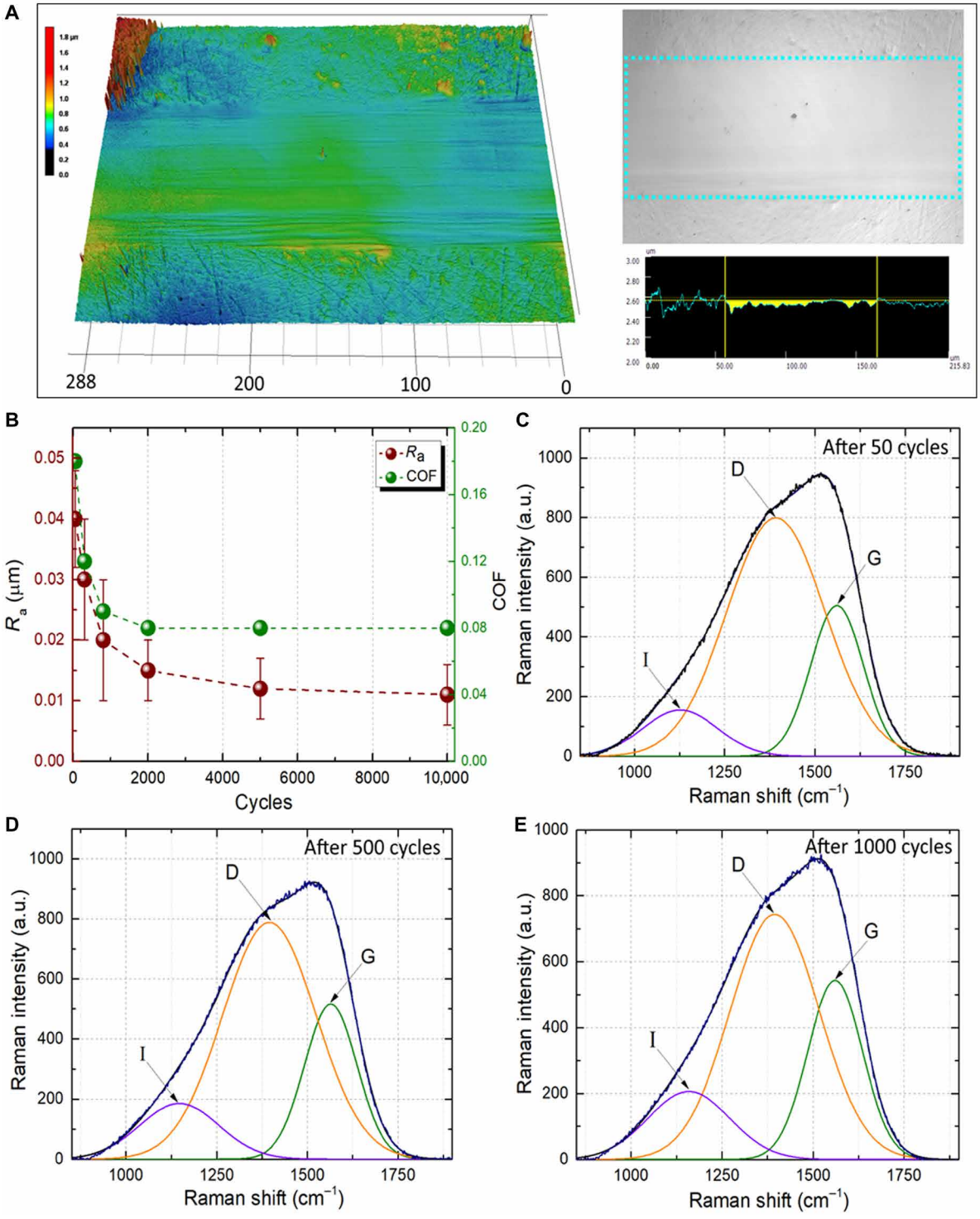

Fig. 6. Wear mechanism and evolution of surface chemistry during sliding. (**A**) Laser confocal microscopy: 3D laser-scanned images, laser-enhanced optical images, and cross-sectional profiles of the wear tracks on Cr20 coating (load, 5 N; dry condition). The area specified by the yellow color indicates the worn area. The blue dashed lines indicate the boundary of the wear tracks. All the dimensions are in micrometers. (**B**) Evolution of R_a and its correlation with COF with respect to the number of cycles. The Raman spectra and Gaussian deconvolutions of the carbon peak of the worn surface after (**C**) 50, (**D**) 500, and (**E**) 1000 cycles. The deconvolutions indicate that the surface became more defective and graphitized as the sliding proceeded.

substrate influenced the von Mises stress contours. In all the cases, the sliding action generated compressive and tensile stress fields in those of regions at the front and behind the tip, respectively. The stress trails can be seen because of the plastic deformation of the substrate. During the sliding, both elastic deformation and plastic deformation occur under the tip, and behind the tip, only the plastic deformation prevails on the surface. In the case of bare HSS, the location of the maximum stress was below the surface as predicted by the contact theory (*56*). Meanwhile, the maximum stress in the substrates underneath the DLC and Cr20 coatings occurred on the surface. This phenomenon can be attributed to the mismatch between the mechanical properties of the coatings and the substrate ($E_{coatings} > E_{substrate}$) (*57*). The plots of the stress values on the surface and along the thickness (at the symmetry plane) of all the substrates are given in Fig. 7 (D and E). These data imply that the surface of the substrate experienced up to 25% lower stress upon reinforcing it by the coatings. The difference was more significant along the thickness. Also, the substrate underneath the Cr20 coating experienced a marginally lower stress (approximately 3%) compared to the substrate underneath the DLC coating.

The state of the stress in the coatings was also investigated. Figure 7 (F and G) shows the von Mises residual stress contours generated in the coatings during loading and sliding. The maximum stress in the coatings was concentrated on the sides, along the edges of the contact zone. To explain this phenomenon, we should consider the parameters that generate the stress field in the coatings: (i) deformation: as a result of plastic behavior of the substrate and the coatings; the plastic deformation results in both compressive and tensile stresses; and (ii) geometry of the deformed regions: The loading and sliding commonly result in formation of pile-ups at the edges of the contact zone (see Fig. 7, H and I) (*58*). According to previous studies (*59*, *60*), an additional bending effect at the edges of the contact zone coating can be caused by the groove geometry and the pile-ups. This bending can, in turn, result in generation of compressive and tensile stresses in addition to the stresses caused by the contact. The substrate yields and pulls down the coating (because the substrate and the coatings are fully bonded). The bending effect here is then caused by both yielding of the substrate and the pile-ups at the edges of the contact zone. In addition, plastic deformation of the substrate also results in releasing the stress at the central region, which shifts the stress concentration toward the edges. Last, plotting the stress profiles along the surface of the coatings (Fig. 7J) shows that the maximum induced stress in the Cr20 coating was lower than the DLC (by approximately 16%). This can be explained by taking the *E* values to consideration wherein the *E* of Cr20 was lower than DLC.

Surface micropatterning

To reduce the wear rate further, the surface patterning technique was used. Studies have reported a pattern density of 5 to 20% as the optimum value for tribological improvements (*61*). In this study as well, the density of dimple-shaped patterns was varied between 5 and 20% by modifying the pitch (*P*) value. Figure 8A illustrates the pulsed fiber laser setup used for fabricating microdimples and a 3D schematic of the geometry of the micropatterns and their corresponding dimensions. Cr20 coating was selected to be deposited on the micropatterned HSS substrates as it showed the highest wear resistance among the coatings. The sliding tests were performed only under lubricated condition because the micropatterning strategy is the most advantageous in terms of friction and wear reduction when used with a lubricant. Also, the sliding tests were performed under the earlier conditions (load, 10 N) for consistency and to enable the assessment of the effects of micropatterning on friction and wear properties and a comparison with the friction and wear properties of Cr20 coating on flat HSS. The *P* values considered in this study were 20, 30, and 40 μm (the corresponding specimens are denoted as P20, P30, and P40 henceforth). The R_a values of P20, P30, and P40 were 170 ± 20, 120 ± 10, and 90 ± 10 nm, respectively (refer to fig. S7 for more information). Figure 8 (B and C) presents the average COFs and wear rates of Cr20 coating on P20, P30, and P40 (in conjunction with those of Cr20 coating on flat HSS as reference and for comparison). As is evident, the COFs of the Cr20 coating on all the microdimpled HSS were lower than that of Cr20 on flat HSS. It was noted that the frictional behavior of Cr20 on P20 differed from that of P30 and P40 in two manners. First, P20 showed a longer running-in period (approximately, 1000 cycles) than P30 (~300 cycles) and P40 (~150 cycles). Second, P20 maintained a marginally lower COF (0.047 to 0.049) than those of P30 (0.048 to 0.052) and P40 (0.05 to 0.055). The running-in behavior can be attributed to the R_a values of the specimens (the higher the R_a, the longer the running-in period became: P20 > P30 > P40). However, this analogy cannot be used to explain why P20 maintained a marginally lower COF than those of P30 and P40 throughout the sliding tests after the running-in period, because the R_a of the worn-out surface on P20 was higher than those for P30 and P40. This implies the involvement of other phenomena in the determination of the friction behavior. This matter is discussed subsequently.

The Cr20 coating on P20 showed a higher wear rate (4.2×10^{-12} $mm^3/N{\cdot}mm$) than that of the Cr20 coating on the flat HSS. As discussed earlier, the wear on P20 appeared in the form of the smoothening of the microasperities. Because a distinct worn area was not apparent (cross-sectional profile in Fig. 8D), the wear rate could be calculated only by subtracting the area of the smoothened asperities from that of the neighboring asperities outside the worn area as reference. In the case of P30, the wear appeared in the form of the smoothening of the nanoasperities. It was not possible to detect any difference between the morphologies of the surfaces inside and outside the wear track according to the profiles obtained by laser confocal microscopy (Fig. 8E). In addition, scanning of the surface using equipment with higher precision and resolution (e.g., atomic force microscope) was not possible owing to the high surface roughness and the high aspect ratio of the microdimples. Therefore, we could estimate the wear rate only based on the information regarding the resolution of the laser confocal microscope. The minimum detectable wear area is specified to be ~0.04 μm^2. Considering this, we assumed that the wear area is less than the specified value, which corresponded to a maximum wear rate of 4×10^{-13} $mm^3/N{\cdot}mm$. We also performed a prolonged wear test under 20,000 cycles in an attempt to obtain a clearer wear profile (see text S9). In the case of P40, the presence of bulges on the worn-out surface made it impossible to assess the wear quantitatively (Fig. 8F; indicated as "nonmeasurable" in Fig. 8C). The R_a values of the worn-out surfaces were 130 ± 10, 110 ± 10, and 110 ± 10 nm for P20, P30, and P40, respectively. The R_a values of P20 and P30 decreased and that of P40 increased, from their respective initial values. These measurements verify our observations of the smoothening of micro- and nanoasperities and formation of bulges in the cases of P20, P30, and P40, respectively.

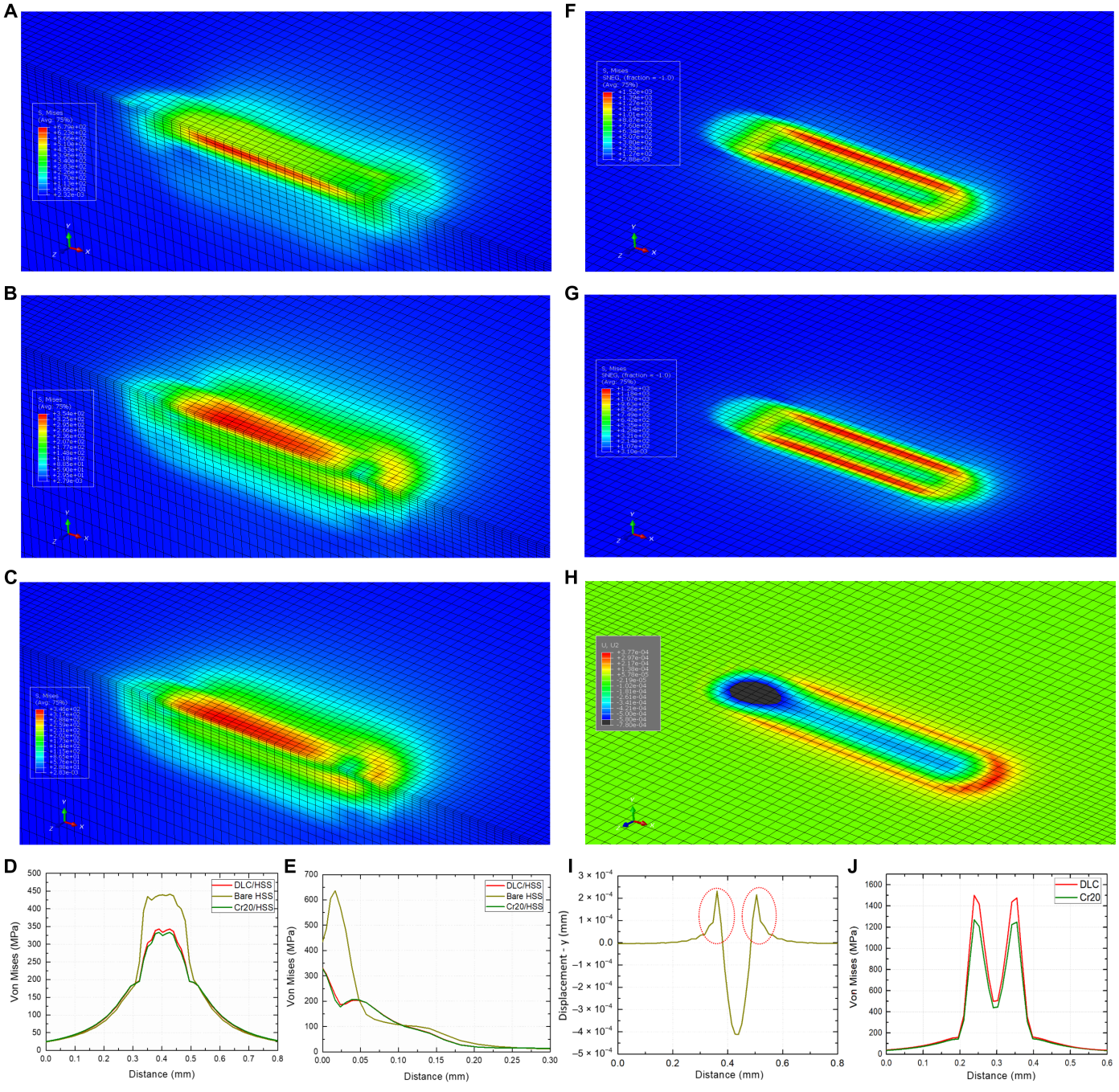

Fig. 7. FE simulations of contact and sliding for the bare and DLC- and Cr20-coated HSS specimens. The sliding direction is from left to right. Topographical von Mises stress-field contours in (**A**) bare HSS, HSS underneath the (**B**) DLC, and (**C**) Cr20 coatings. Numerical comparison of the von Mises stress values (**D**) on the surface and (**E**) along the thickness (at the symmetry plane) of the substrates. Topographical von Mises stress-field contours in the (**F**) DLC and (**G**) Cr20 coatings. (**H**) Field map showing the vertical deformation of the bare HSS substrate (along the *y* axis). The dark-gray region indicates the point of initial indentation before sliding and convergence of the load to 10 N. (**I**) Deformation profile of the bare HSS substrate. The pile-ups at the edges of the contact zone are specified by the dashed red circles. (**J**) Numerical comparison of the generated von Mises stress values on the surface for the DLC and Cr20 coatings.

The Hersey number was calculated to be ~0.00014. The marginal value of the Hersey number and the range of COF values indicated that the sliding tests were performed mainly in the boundary lubrication regime (*62*, *63*). COF values in the range of 0.04 to 0.1 in the boundary lubrication condition for coated or bare patterned surfaces have also been reported (*64*, *65*). The lubrication regime can be explained by considering the sliding conditions and the state of the micropatterned surfaces. The sliding tests were performed under a high normal load and low sliding velocity (10 N and 8 mm/s). These conditions can promote boundary lubrication (*64*, *66*). The

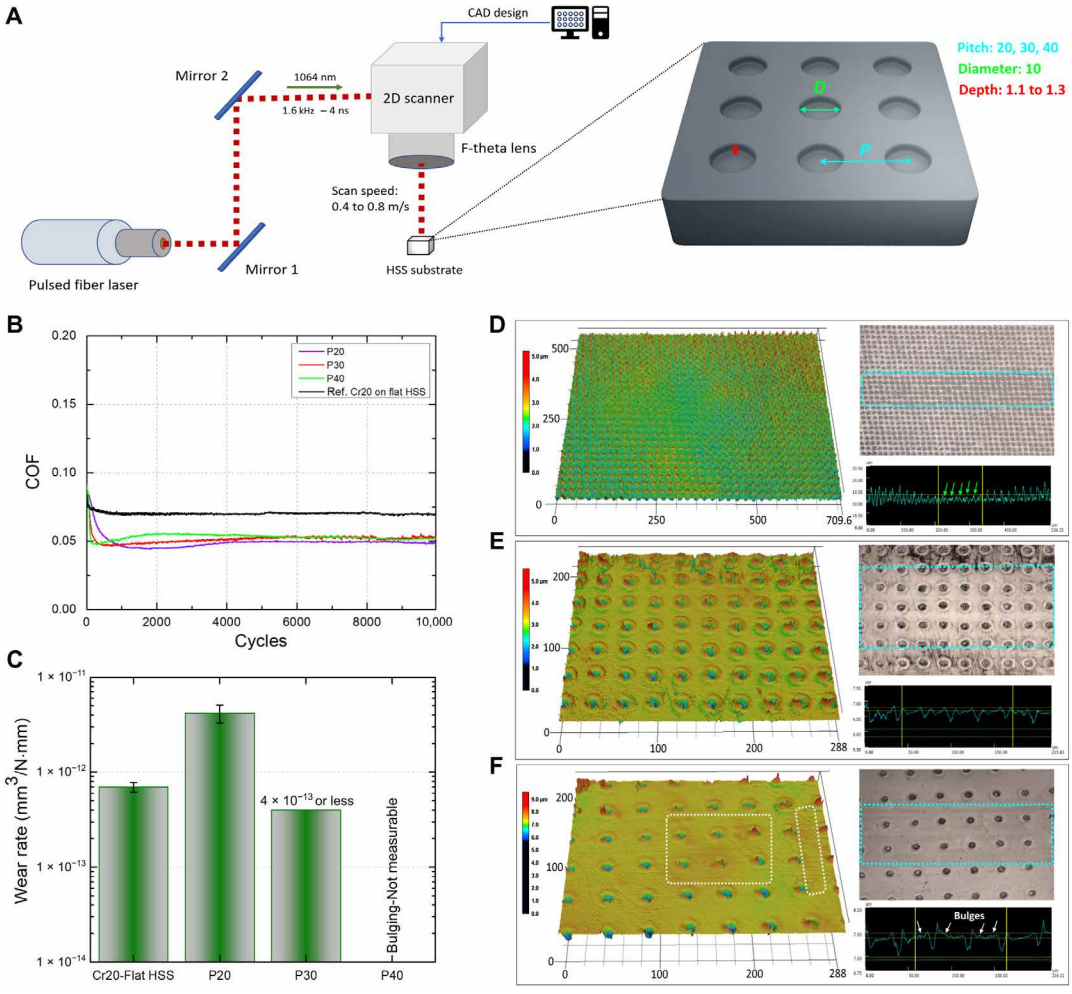

Fig. 8. Pulsed fiber laser fabrication setup, visualization of the wear tracks, and macrotribological properties. (**A**) Schematic of the lasing setup used for fabrication of microdimples on HSS. The lasing procedure was done in one cycle with a frequency and pulse duration of 1.6 kHz and 4 ns, respectively. Variations of (**B**) COF with respect to sliding cycles, and (**C**) wear rates of Cr20 coating on micropatterned HSS. The COF and wear rate of Cr20 on flat HSS are also given as reference. 3D laser-scanned images, laser-enhanced optical images, and cross-sectional profiles of the wear tracks on (**D**) P20, (**E**) P30, and (**F**) P40. The blue dashed lines indicate the boundary of the wear tracks. Green arrows in (D) indicate the smoothened microasperities. White dashed lines and arrows in (**F**) specify the formation of bulges on the worn surface. Load, 10 N; lubrication condition. All the dimensions are in micrometers.

formation of burrs around the edge of the micropatterns (see text S6) and increased surface roughness upon micropatterning were other reasons for lubrication in the boundary regime (*64*, *66*, *67*). It should be noted that variation in the density of the micropatterns may affect the mixed and hydrodynamic components of the lubrication to a certain degree as well. This matter is elaborated further in Discussion.

DISCUSSION

According to our benchmarks (tables S3 and S4), despite having a lower thickness, the COF and wear rate of the Cr20 coating are substantially lower than those reported values at the macroscale by date. A lower thickness is beneficial in certain situations wherein large thickness of the coatings may hinder their applications or degrade their functionality (*3*). Such wear behavior can be explained by considering the phenomena associated with varying the Cr deposition power. An increase in the deposition power enhances the electric field perpendicular to the target plane. This, in turn, increases the plasma density and ionization. The bombarding ions (Ar+) gain more kinetic energy/momentum and transfer their momentum to the target atoms upon impact. This results in a higher kinetic energy of the atoms/ions ejected from the target (*68*). The increased kinetic energy of the ejected Cr atoms affected the structure of the nanolayered coatings in four manners: (i) The level of intermixing at the Cr/DLC interface increased. (ii) The growth mechanism of Cr nanolayers: Deposition at a higher sputtering power may result in coating growth in the VW or SK mode (*16*, *17*). It has also been reported that coatings prepared with higher deposition powers exhibit a higher degree of crystallinity that is consistent with the characteristics of coatings grown in the VW or SK mode (*16*). This agrees with our observations from the HR-TEM analysis, wherein more nanocrystalline phases started to form as the Cr deposition power reached 120 W. The higher degree of crystallinity of Cr nanolayers in Cr150 coating can be also explained by considering the overall thickness of individual Cr layers. Metallic elements tend

to readily crystallize if their thickness exceeds a critical threshold. For example, this critical threshold has been determined to be approximately 4 nm for Co in a Co/DLC multilayer system (*6*). The critical thickness for Cr in our Cr/DLC nanolayered system was ~2 nm. (iii) The roughness and morphology at the interface of the nanolayers: The increased roughness, nonuniformity, and formation of wavy nanointerfaces is a consequence of growth mode transition and the stress induced by the formation of islands. (iv) Quantity and type of defects/disorders in the DLC nanostructure: This phenomenon can be explained by considering the growth mechanisms, physics of the sputtering process, and kinetic energy of the ejected Cr atoms/ions. At high deposition powers ($\geq$ 40 W), the Cr adatoms/ions have the energy necessary to disrupt sp^2 or sp^3 carbon bonds of the underlying DLC nanolayers upon impact. The type of the disruption caused in the DLC nanostructure depends on the extent of kinetic energy. In addition, a higher momentum of ejected Cr atoms implies that more energy would be converted to heat upon impact with the underlying carbon atoms (given the fixed deposition time, the higher the Cr deposition power, the higher the temperature of the underlying DLC layers becomes). DLC tends to graphitize (more sp^2 bonds) at elevated temperatures (*69*). This is consistent with our Raman analysis, wherein the percentage of sp^3 content decreased as the Cr deposition power increased. Figure 9A provides a schematic comparison, according to the above discussion, between those of classic periodic nanolayered coatings and the Cr20 coating. For a detailed discussion regarding the Cr20-10s coating, refer to text S7.

A comprehensive model to describe the wear behavior must consider both structural features at the atomic level (obtained from Raman analysis) and mechanical properties (determined by nanoindentation analysis) of the coatings. It should be noted that defining a model based on dependent parameters from each analysis affects the reliability of the model. For example, it is established that the percentage of sp^3 bonds in DLC is highly correlated with its hardness (variations in the sp^3 content would reflect on the hardness). Therefore, these two parameters cannot be used together in a model. Considering this, we proposed a model based on the independent parameters from each analysis. We defined a dimensionless parameter (denoted with $\mathbb{K}$) that is the quotient of $A(D + D')$ and H/E. As discussed earlier, $A(D + D')$ represents the quantity of atomic defects. Meanwhile, H/E effectively represents the mechanical response of the coatings under contact condition as a measure of elasticity. Variations in H/E also reflect on the variations in the sp^3 content or the formation of carbide (CrC_x) phases with respect to the Cr deposition power. Both the defect density and elasticity are known to strongly affect the wear properties (*49*, *55*). Our data in Figs. 3 and 4 indicate that these parameters do not influence each other and hence can be used together in a model. It should be noted that certain studies have reported a relationship between hardness and nanostructural defects of the same type (*70*, *71*). However, this was not the case in this study because the variations in the Cr deposition power not only changed the quantity of the defects but also altered their type.

Figure 9B presents the dependency of the wear rates on $\mathbb{K}$ (the lower $\mathbb{K}$ is, the lower is the wear rate). As is evident, the wear rate values well follow the variations in $\mathbb{K}$ with respect to the Cr deposition power. A correlation coefficient of ~0.82 was obtained between $\mathbb{K}$ and wear rate. This demonstrates the high dependency of wear rate on $\mathbb{K}$. The $\mathbb{K}$ value of Cr20 coating was significantly lower than those of the remaining coatings. However, an irregularity between the wear rate of DLC and its $\mathbb{K}$ compared with the cases of the Cr40, Cr80, and Cr120 coatings is evident. The $\mathbb{K}$ value obtained for DLC was higher than that for Cr40 (almost equal to that for Cr80 and Cr120), whereas its wear rate was lower than that of the coatings. This indicates the involvement of chemical phenomena in the determination of the wear behavior. To investigate, the countersurfaces (steel balls) were analyzed using laser confocal microscopy and Raman spectroscopy (see text S8). The analysis revealed that the contact zones were covered with what appeared to be a substance/film (known as tribo-film) whose characteristics differed from those of the deposited coatings. Three main conclusions were drawn on the basis of the Gaussian deconvolutions: (i) The tribo-film that was formed on the ball that slid on DLC showed higher FWHM(G) compared with those of the tribo-film formed on the balls that slid on Cr40, Cr80, and Cr120. This implied that the tribo-film that corresponded to DLC potentially contained more sp^3 bonds, which resulted in a higher level of protection against wear. (ii) The tribo-films in the case of the balls that slid on Cr120 and Cr150 were discontinuous. This could be attributed to the higher degree of abrasive wear at a higher Cr deposition power as discussed previously. In this case, the tribo-film did not play a significant role in the protection of the contact pairs against wear. These two conclusions may explain the presence of the abovementioned irregularity. (iii) The $I(G)$ of the tribo-film formed on the ball that slid on Cr20 coating (under both 5 and 10 N) was smaller than that of the remaining tribo-films. This implies that the tribo-film was mainly amorphous carbon and that the level of graphitization caused by pressure and shear stress during the wear tests was less than those for the other tribo-films.

A correlation coefficient of ~0.96 between the $\mathbb{K}$ parameter and wear rates is obtained if we exclude DLC. The high values of the correlation coefficients imply that our proposed model not only explains the exceptionally low wear rate of Cr20 coating but also can be used to effectively predict the wear rate of carbon-based nanolayered coatings providing that the difference in the chemistry of the tribo-films for those of coatings that are being compared remains insignificant. As $\mathbb{K}$ takes the chemistry of the coatings to consideration, it is a more comprehensive criterion compared to those of classic criteria for describing the wear properties such as H/E and H^3/E^2. Moreover, because $\mathbb{K}$ is defined on the basis of the defects and disorders of carbon, it is suggested that it can be used to represent the wear behavior of other carbon-based nanolayered coatings as well. However, more research on various material pairs (other than Cr) for carbon should be performed before generalizing the applicability of this parameter.

To analyze the macrotribological properties of the Cr20 coating on the microdimpled substrates, we should review the fundamental mechanisms by which surface patterning improves tribological properties. In general, surface patterning can lower friction and wear, mainly through five different mechanisms: (i) by reducing the real area of contact (RAC); (ii) by trapping the wear debris generated during sliding (eliminates stress concentration and wear caused by abrasion and ploughing); (iii) by serving as microreservoirs for lubricant (RL) (ensures the continuous supply of lubricant throughout the sliding and alters the lubrication regime to mixed lubrication (*64*); (iv) by increasing the adhesion of coating to the substrate by deflecting the propagation of interfacial cracks and, thereby, suppressing the delamination failure during wear (*72*); and (v) by generating a hydrodynamic pressure (HP) between the surfaces in

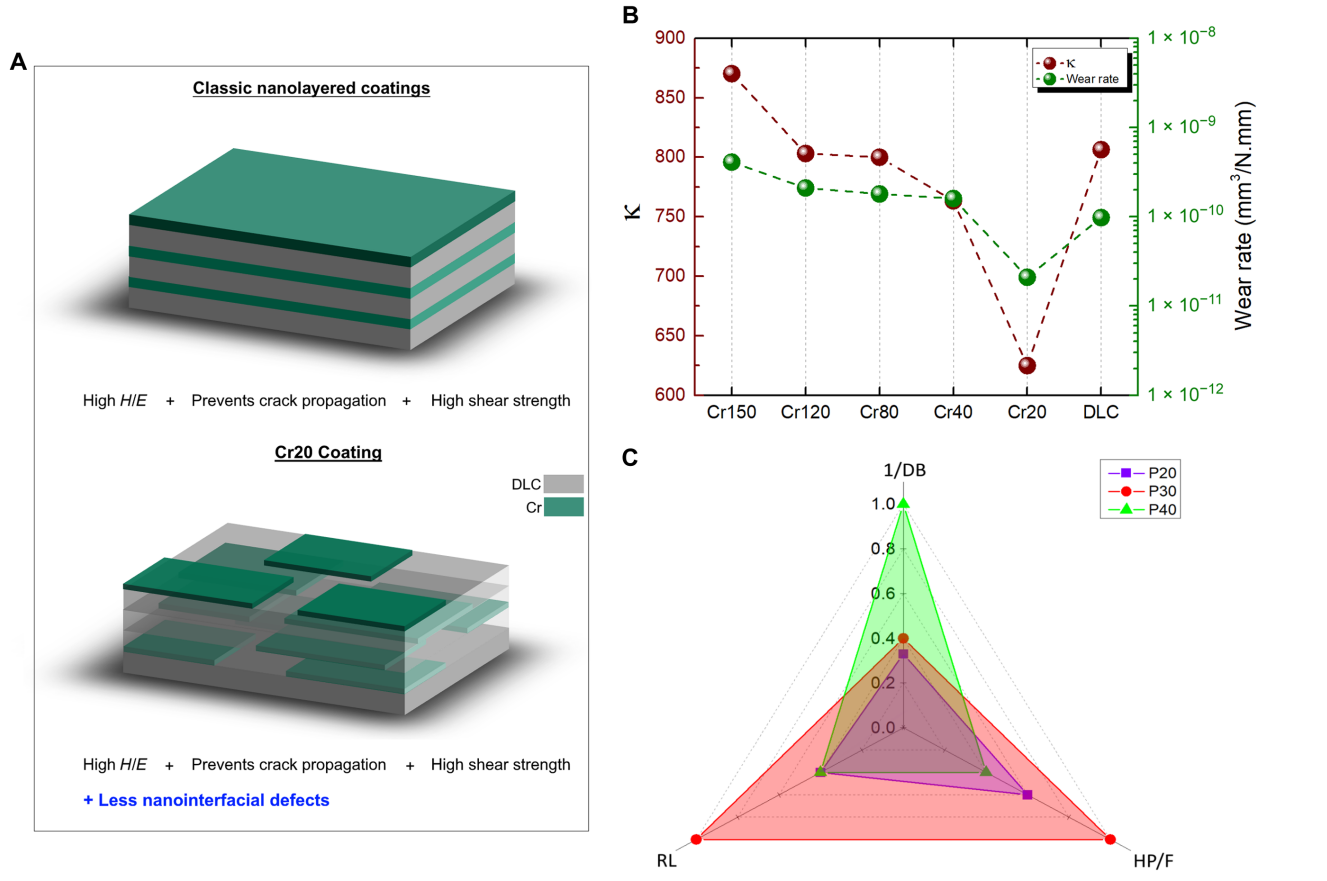

Fig. 9. Proposed models to describe the wear behaviors. (**A**) Schematic representation of the nanostructure of those of classic periodic nanolayered coatings and Cr20 coating. (**B**) Dependency of wear rate on the proposed dimensionless K parameter [defined as the quotient of $A(D + D')$ and H/E by this study]. A direct correlation between K and wear rate is observed. (**C**) Characteristics of P20, P30, and P40 in terms of the parameters affecting the tribological properties. To enable comparison of the parameters, the values are normalized (>0 and ≤1, with 1 being the most favorable to the wear resistance).

contact owing to the entrapment and compression of lubricant inside the micropatterns (functioning as microhydrodynamic bearings) that can result in lift-off effect and, thereby, a certain increase in the load carrying capacity (*73*). In boundary lubrication, the contact bodies are separated by only a few layers of molecules, and the film varies in thickness from one to a few tens of nanometers. Provided that a sufficient amount of lubricant is supplied, a marginal degree of HP is likely to be generated by the constant and continuous entrapment and compression of lubricant inside the micropatterns upon contact (*67*). Each of the abovementioned mechanisms is highly dependent on the characteristics of the micropatterns [*D*, *P*, and volume of dimples (*V*)]. A variation in *P* results in a variation in the number of dimples (*N*) and the density of burrs (DB) along the width of the wear track. This, in turn, causes the RAC and amount of RL to vary, and therefore, the expected HP varies. To simplify, the characteristics of P20, P30, and P40 in terms of the parameters defined above are listed in Table 1.

RAC and RL are proportional to *D* and *V*, respectively. Meanwhile, the correlation between HP and the geometry of the fabricated microdimples is more complex. A close inspection of the cross-sectional profiles of the fabricated microdimples reveals that the bottom end of the microdimples on P20 is sharp. This makes these more conical unlike the microdimples on P30 and P40, which are flat-end and more cylindrical (refer to fig. S7). Numerical and experimental studies have shown that cylindrical dimples generate a 40 to 60% higher load carrying capacity compared with that of conical dimples (*74*, *75*). This phenomenon occurs because the wedge divergence in the conical dimples is gentler than that in the cylindrical dimples (*74*). Therefore, assuming that the individual microdimples on P30 and P40 generate an equal HP owing to their geometrical similarities, individual microdimples on P20 can generate 0.4 to 0.6 HP (an average of 0.5 HP). It should be mentioned that the fabrication of conical microdimples on P20 was unintentional and only owing to the slow scanning speed. For the higher speeds, the advancement of a pulse during a pulse duration (4 ns) becomes prominent. Hence, the microdimples in the case of P30 and P40 have a cylindrical shape.

As discussed previously, the initial R_a values (as a result of formation of burrs) showed a direct relationship with the running-in period. This is because the rate of material removal is highest during the running-in period (*41*). After the running-in period, the Cr20 coating on P20 showed a COF that was marginally lower than those of P30 and P40. The lower COF in this case can be attributed to a lower RAC because of the higher density of microdimples on P20. The effect of RAC on the COF of P30 and P40 was also evident. Here, the Cr20 coating on P30 showed a slightly lower COF than

Table 1. Characterization of P20, P30, and P40 specimens in terms of characteristics of the microdimples involved in the determination of the friction and wear behavior.

Specimen	Initial R_a (nm)	N	DB	RAC	RL	HP
P20	170 ± 20	6	∝6	$\propto N \times D^2$	$N \times V/3$	$\propto \sim 50\% \times N$
P30	120 ± 10	5	∝5	$\propto N \times D^2$	$N \times V$	$\propto N$
P40	90 ± 10	2	∝2	$\propto N \times D^2$	$N \times V$	$\propto N$

that for P40. However, it should be noted that although favorable to COF, less RAC does not always correspond to a lower wear because the contact stress increases as the RAC decreases. As pointed out earlier, studies have shown that the amount of wear is the minimum for a specific density (not necessarily the highest density) of micropatterns.

A comprehensive model to describe the macrotribological properties should consider all the abovementioned parameters. Figure 9C presents the established correlations between the defined parameters for P20, P30, and P40 and their corresponding wear behavior. The effect of individual parameters on wear behavior can be visually assessed using this plot. The calculation of the area of the triangles for P20, P30, and P40 produces a dimensionless value that has a direct relationship with the macrotribological properties and can be used as a criterion to measure and predict the wear performance of Cr20 coating on microdimpled specimens. The integrated areas of the triangles are in the following order: P30 > P40 > P20. This implies a higher capacity of P30 for improving the macrotribological properties of Cr20 coating as demonstrated by the data.

Conclusion

We comprehensively discussed the effects of the properties of nanoscale interfaces including the growth mode of Cr nanolayers, quantity and origin of defects, and degree of intermixing on macrotribological properties of DLC/Cr periodic nanolayered coatings. The characteristics of the nanointerfaces were tailored using our patented deposition technique by varying the Cr sputtering power (from 20 to 150 W) while maintaining a deposition time of 4 s. An evident transition in the growth mode of Cr nanolayers from FM to SK was observed at 80 W. This phenomenon deteriorated the wear resistance of the coatings. Through the engineering and optimization of the nanointerfaces, a new class of coating with subnanometer-thick periodic albeit discrete interlayers for macrotribological applications was fabricated. This coating not only had all the features of classic multilayer coatings but also contained lower nanointerfacial defects. As a result, a lower COF and record-breaking wear rates at the macroscale under different sliding conditions (dry, lubricated, and lubricated + micropatterned) were achieved. According to the FE simulations, the Cr20 coating reduced the stress induced in the substrate during contact and sliding by ~25% and showed by ~16% lower stress compared to the DLC coating. We also report on the discovery of a dimensionless parameter (Ƙ) that is more comprehensive compared to those of classic criteria and can be used to effectively explain and predict the wear behavior of carbon-based nanolayered coatings. The results of this study strongly imply that growth of the coating materials according to the first stage of FM mode must be acknowledged as an additional criterion to construct the periodic nanolayered coatings for macrotribological applications. The findings in this paper open new windows with regard to the design concepts of nanolayered coatings for tribological applications by establishing important connections between the nanostructural characteristics and the macroscale properties.

MATERIALS AND METHODS

Deposition of nanolayered coatings

To improve the adhesion between coatings and substrates, the surface oxide layer on HSS (refer to text S1 for more information regarding the HSS substrate) was removed before coating deposition using argon (Ar) plasma treatment inside a load lock chamber for 20 min at 40 W. Cr as an adhesion layer was deposited onto the HSS substrates before DLC deposition. A sample holder moved the substrates alternatively beneath the graphite and Cr targets (99.99% purity). The deposition time was controlled using an automatic shutter, which moved alternatively with the sample holder. The DLC and Cr coatings were deposited using a pulsed DC (250 mA and 40 kHz) and automatic RF power, respectively. It should be noted that deposition of Cr at powers below 20 W was not possible owing to the instability of plasma discharge. The base pressure before deposition was 4×10^{-6} torr. The coatings were deposited in an Ar gas atmosphere (flow rate, 10 sccm). A fully automatic throttle valve controlled and maintained the working pressure at 2×10^{-3} torr during the deposition.

Micro/nanostructure evaluation

The state of the nanostructure and chemical characteristics of the coatings were investigated using XRD (Cu source; wavelength of 0.154 nm), LAXRD, (AR-) XPS, EDS, and Raman spectroscopy (laser wavelength = 532 nm). The nanostructure of the coatings was visualized using HR-TEM. The surface morphology and wear tracks were analyzed using laser confocal microscopy with a laser wavelength of 408 nm in the ultrahigh-precision mode. To assess the mechanical properties of the coatings, two series of nanoindentations were performed using a high-precision ultra-nanoindenter. The first series of indentations was performed using a standard diamond Berkovich tip to obtain the H and E of the coatings. The indentation load was set to 5 mN. To prevent the substrate effect, the maximum indentation depth was adjusted to be less than 10 to 15% of the total coating thickness. The second series of nanoindentations were performed using a spherical diamond tip (radius, 20 μm) to assess the elastic/plastic behavior of the coatings and obtain their true stress–true strain curves to be used as input to FE simulations. The indentation load was varied from 5 to 50 mN. The average residual compressive stress of the coatings was quantified using Stoney's equation (*50*). The curvature of the coatings required for stress calculations was obtained through scanning of the surfaces using a profilometer (tip diameter, 0.7 μm).

Friction and wear tests

To assess the friction properties and wear resistance of the specimens, a series of sliding tests were conducted using a custom-built reciprocating macrotribometer. The sliding tests were performed under both dry and lubricated conditions. A fully synthetic oil was used as the lubricant (viscosity, ~180 mPa·s at 25°C) and was delivered to the contact interface using a syringe injector before starting the sliding test to fully cover the contact region throughout the duration of the test. Steel balls (SS304) with a diameter of 5 mm were used as countersurfaces. The corresponding contact pressures generated under the normal loads of 5 and 10 N were ~1.26 and ~1.60 GPa, respectively, based on the Hertzian theory (*56*). The sliding speed and stroke were 8 mm/s and 2 mm, respectively. The humidity and room temperature were monitored throughout the sliding tests (55 ± 5% and 25° ± 3°C, respectively). Each sliding test was repeated at least three times. The amount of wear was quantified in terms of the wear rate ($mm^3\ N^{-1}\ mm^{-1}$) based on Archard's equation (*76*). The wear area was obtained using laser confocal microscopy by averaging the profile at multiple cross sections.

FE simulations

To accurately simulate the behavior of the specimens under contact/sliding condition, the data obtained from the experiments were incorporated into the modeling process, plastic properties (obtained from ultra-nanoindentations), friction coefficient (obtained from sliding tests), and the actual thickness of the coatings. The simulations involved four main steps: (i) contact: the tip moved down toward the substrate surface until contact was established; (ii) relaxation: the contact depth was adjusted until the normal load was merged to the defined value of 10 N; (iii) sliding: the tip rubbed against the surface while maintaining the normal load of 10 N; and (iv) lift-off: the tip moved up and detached from the substrate surface.

Fabrication of microdimples

Dimple-shaped micropatterns with an average diameter (D) of 10 μm were fabricated on HSS substrates using an Ytterbium-doped pulsed nanosecond fiber laser (YLPM-1-4 × 200-20-20) with a wavelength of 1064 nm. An average output power of 200 mW was used. The scanning speeds were set to 0.4 (P20), 0.6 (P30), and 0.8 m/s (P40) to obtain the intended pitch values. The above-mentioned P values resulted in pattern densities of approximately 20%, 10%, and 5% for P20, P30, and P40, respectively. It should be mentioned that the values for D and P were selected such that a sufficient number of dimples could fit inside the wear track.

SUPPLEMENTARY MATERIALS

Supplementary material for this article is available at https://science.org/doi/10.1126/sciadv.abk1224

REFERENCES AND NOTES

1. K. Holmberg, A. Erdemir, Influence of tribology on global energy consumption, costs and emissions. *Friction* **5**, 263–284 (2017).
2. K. Holmberg, P. Kivikytö-Reponen, P. Härkisaari, K. Valtonen, A. Erdemir, Global energy consumption due to friction and wear in the mining industry. *Tribol. Int.* **115**, 116–139 (2017).
3. N. Dwivedi, R. J. Yeo, C. Dhand, J. Risan, R. Nay, S. Tripathy, S. Rajauria, M. S. M. Saifullah, S. K. R. S. Sankaranarayanan, H. Yang, A. Danner, C. S. Bhatia, Boosting contact sliding and wear protection via atomic intermixing and tailoring of nanoscale interfaces. *Sci. Adv.* **5**, eaau7886 (2019).
4. A. F. S. Baharin, M. J. Ghazali, J. A. Wahab, Laser surface texturing and its contribution to friction and wear reduction: A brief review. *Ind. Lubr. Tribol.* **68**, 57–66 (2016).
5. M. Khadem, O. V. Penkov, H. K. Yang, D. E. Kim, Tribology of multilayer coatings for wear reduction: A review. *Friction* **5**, 248–262 (2017).
6. O. V. Penkov, A. U. Devizenko, M. Khadem, E. V. Zubarev, V. V. Kondratenko, D.-E. Kim, Toward zero micro/macro-scale wear using periodic nano-layered coatings. *ACS Appl. Mater. Interfaces* **7**, 18136–18144 (2015).
7. K. A. Lozovoy, A. G. Korotaev, A. P. Kokhanenko, V. V. Dirko, A. V. Voitsekhovskii, Kinetics of epitaxial formation of nanostructures by Frank–van der Merwe, Volmer–Weber and Stranski–Krastanow growth modes. *Surf. Coat. Technol.* **384**, 125289 (2020).
8. A. Pimpinelli, J. Villain, *Physics of Crystal Growth* (Cambridge University Press, 2010).
9. J. E. Greene, Thin film nucleation, growth, and microstructural evolution: An atomic scale view, in *Handbook of Deposition Technologies for Films and Coatings* (William Andrew, ed. 3, 2010), pp. 554–620.
10. H. Fujioka, Pulsed laser deposition (PLD), in *Handbook of Crystal Growth: Thin Films and Epitaxy* (Elsevier, ed. 2, 2015), pp. 365–397.
11. K. Oura, V. G. Lifshits, A. Saranin, A. V. Zotov, M. Katayama, *Surface Science: An Introduction* (Springer, 2003).
12. C. I. Fornari, G. Fornari, P. H. Rappl, E. Abramof, J D. S. Travelho, Monte Carlo simulation of epitaxial growth, in *Epitaxy* (Intech, 2018), pp. 115–129.
13. O. V. Penkov, I. A. Kopylets, V. V. Kondratenko, M. Khadem, Synthesis and structural analysis of Mo/B periodical multilayer X-ray mirrors for beyond extreme ultraviolet optics. *Mater. Des.* **198**, 109318 (2021).
14. M. Jung, E. Lee, D. Kim, K. Kim, C. Yun, H. Lee, H. Kim, K. Rhie, S. Jeon, Amorphous FeZr metal for multi-functional sensor in electronic skin. *Npj Flex. Electron.* **3**, 8 (2019).
15. Y. S. Kim, H. J. Park, K. S. Lim, S. H. Hong, K. B. Kim, Structural and mechanical properties of AlCoCrNi high entropy nitride films: Influence of process pressure. *Coatings* **10**, 10 (2020).
16. M. Khan, M. Islam, Deposition and characterization of molybdenum thin films using dc-plasma magnetron sputtering. *J. Semicond.* **47**, 1610–1615 (2013).
17. A. I. Oje, A. A. Ogwu, M. Mirzaeian, N. Tsendzughul, A. M. Oje, Pseudo-capacitance of silver oxide thin film electrodes in ionic liquid for electrochemical energy applications. *J. Sci. Adv. Mater. Dev.* **4**, 213–222 (2019).
18. A. Kumar, V. Kumar, R. Chandra, Y. K. Gautam, Effect of sputtering process parameters on structural and optical properties of CdS thin films. *Mater. Res. Express* **6**, 106448 (2019).
19. N. Kaiser, Review of the fundamentals of thin-film growth. *Appl. Optics* **41**, 3053–3060 (2002).
20. L. B. Freund, S. Suresh, *Thin Film Materials: Stress, Defect Formation and Surface Evolution* (Cambridge Univ. Press, 2010).
21. J. Venables, *Introduction to Surface and Thin Film Processes* (Cambridge Univ. Press, 2010).
22. A. A. Voevodin, S. D. Walck, J. S. Zabinski, Architecture of multilayer nanocomposite coatings with super-hard diamond-like carbon layers for wear protection at high contact loads. *Wear* **203-204**, 516–527 (1997).
23. X. Zhang, Y. Wu, B. Xu, H. Wang, Residual stresses in coating-based systems, part II: Optimal designing methodologies. *Front. Mech. Eng. China* **2**, 125–136 (2007).
24. N. Nemati, M. Bozorg, O. V. Penkov, D. G. Shin, A. Sadisghzadeh, D.-E. Kim, Functional multi-nanolayer coatings of amorphous carbon/tungsten carbide with exceptional mechanical durability and corrosion resistance. *ACS Appl. Mater. Interfaces* **9**, 30149–30160 (2017).
25. H. Jiang, H. Wang, J. Zhu, C. Xue, J. Zhang, N. Tian, A. Li, Thickness-dependent structural characteristics for a sputtering-deposited chromium monolayer and Cr/C and Cr/Sc multilayers. *J. Synchrotron Radiat.* **25**, 785–792 (2018).
26. D.-E. Kim, V. S. Dhandapani, K.-J. Seo, Metal-Containing DLC Film and Manufacturing Method Thereof, Korean Patent Registration No. 10–2081264 (2020).
27. V. S. Dhandapani, K. M. Kang, K. J. Seo, C. L. Kim, D. E. Kim, Enhancement of tribological properties of DLC by incorporation of amorphous titanium using magnetron sputtering process. *Ceram. Int.* **45**, 11971–11981 (2019).
28. K. Nygren, M. Samuelsson, A. Flink, H. Jungcrantz, Å. K. Rudolphi, U. Jansson, Growth and characterization of chromium carbide films deposited by high rate reactive magnetron sputtering for electrical contact applications. *Surf. Coat. Technol.* **260**, 326–334 (2014).
29. C. Mitterer, M. Lechthaler, G. Gassner, G. A. Fontalvo, L. Tóth, B. Pécz, M. Raible, K. Maier, E. Bergmann, Self-lubricating chromium carbide/amorphous hydrogenated carbon nanocomposite coatings: A new alternative to tungsten carbide/amorphous hydrogenated carbon. *Proc. Inst. Mech. Eng. Part J J. Eng. Tribol.* **223**, 751–757 (2009).
30. G. Gassner, J. Patscheider, P. H. Mayrhofer, E. Hegedus, L. Tóth, I. Kovacs, B. Pécz, V. Srot, C. Scheu, C. Mitterer, Structure of sputtered nanocomposite CrC_x/a-C:H thin films. *J. Vac. Sci. Technol. B* **24**, 1837–1843 (2006).
31. C. Quan, Y. He, Properties of nanocrystalline Cr coatings prepared by cathode plasma electrolytic deposition from trivalent chromium electrolyte. *Surf. Coat. Technol.* **269**, 319–323 (2015).
32. C. S. Casari, A. L. Bassi, A. Baserga, L. Ravagnan, P. Piseri, C. Lenardi, M. Tommasini, A. Milani, D. Fazzi, C. E. Bottani, P. Milan, Low-frequency modes in the Raman spectrum of sp–sp^2 nanostructured carbon. *Phys. Rev. B* **77**, 195444 (2008).

33. S. E. Rodil, A. C. Ferrari, J. Robertson, W. I. Milne, Raman and infrared modes of hydrogenated amorphous carbon nitride. *J. Appl. Phys.* **89**, 5424 (2001).
34. D. Roy, M. Chhowalla, H. Wang, N. Sano, I. Alexandrou, T. W. Clyne, G. A. J. Amaratunga, Characterisation of carbon nano-onions using Raman spectroscopy. *Chem. Phys. Lett.* **373**, 52–56 (2003).
35. F. Li, J. S. Lannin, Disorder induced Raman scattering of nanocrystalline carbon. *Appl. Phys. Lett.* **61**, 2116–2118 (1992).
36. R. Shuker, R. W. Gammon, Raman-scattering selection-rule breaking and the density of states in amorphous materials. *Phys. Rev. Lett.* **25**, 222–225 (1970).
37. G. Pezzotti, C. Camara, E. Marin, W. Zhu, D. Green, A. Collins, S. Putterman, Physical chemistry insights into surface charge phenomena during frictional coupling in triboelectric X-ray sources. *J. Mater. Chem. C* **7**, 7708–7724 (2019).
38. A. C. Ferrari, J. Robertson, Origin of the 1150–cm^{-1} Raman mode in nanocrystalline diamond. *Phys. Rev. B* **63**, 121405 (2001).
39. A. C. Ferrari, J. Robertson, Raman spectroscopy of amorphous, nanostructured, diamond-like carbon, and nanodiamond. *Phil. Trans. R. Soc. A* **362**, 2477–2512 (2004).
40. A. Michau, F. Maury, F. Schuster, R. Boichot, M. Pons, E. Monsifrot, Chromium carbide growth at low temperature by a highly efficient DLI-MOCVD process in effluent recycling mode. *Surf. Coat Technol.* **332**, 96–104 (2017).
41. M. Khadem, D. E. Kim, Friction and wear behaviors of bare and diamond-like carbon/chromium bi-layer coated SKH51 steel at low temperatures. *Surf. Coat Technol.* **412**, 127018 (2021).
42. Z. Wu, Z. Ni, Spectroscopic investigation of defects in two-dimensional materials. *Nanophotonics* **6**, 1219–1237 (2017).
43. F. Rosenburg, E. Ionescu, N. Nicoloso, R. Riedel, High-temperature Raman spectroscopy of nano-crystalline carbon in silicon oxycarbide. *Materials* **11**, 93 (2018).
44. M. Kahn, M. Čekada, T. Schöberl, R. Berghauser, C. Mitterer, C. Bauer, W. Waldhauser, E. Brandstätter, Structural and mechanical properties of diamond-like carbon films deposited by an anode layer source. *Thin Solid Films* **517**, 6502–6507 (2009).
45. C. Casiraghi, A. C. Ferrari, J. Robertson, Raman spectroscopy of hydrogenated amorphous carbons. *Phys. Rev. B* **72**, 85401 (2005).
46. W. G. Cui, Q. B. Lai, L. Zhang, F. M. Wang, Quantitative measurements of sp^3 content in DLC films with Raman spectroscopy. *Surf. Coat. Technol.* **205**, 1995–1999 (2010).
47. A. Eckmann, A. Felten, A. Mishchenko, L. Britnell, R. Krupke, K. S. Novoselov, C. Casiraghi, Probing the nature of defects in graphene by Raman spectroscopy. *Nano Lett.* **12**, 3925–3930 (2012).
48. W. C. Oliver, M. C. Pharr, Measurement of hardness and elastic modulus by instrumented indentation: Advances in understanding and refinements to methodology. *Mater. Res.* **19**, 3–20 (2004).
49. H. K. Yang, M. Khadem, O. V. Penkov, D. E. Kim, Increased elasticity and damping capacity of diamond-like carbon coatings by immobilized C_{60} fullerene clusters. *Nanoscale* **11**, 2863–2870 (2019).
50. G. Abadias, E. Chason, J. Keckes, M. Sebastiani, G. B. Thompson, E. Barthel, G. L. Doll, C. E. Murray, C. H. Stoessel, L. Martin, Review Article: Stress in thin films and coatings: Current status, challenges, and prospects. *J. Vac. Sci. Technol.* **36**, 020801 (2018).
51. Y. M. Hu, J. Y. Li, N. Y. Chen, C. Y. Chen, T. C. Han, C. C. Yu, Effect of sputtering power on crystallinity, intrinsic defects, and optical and electrical properties of Al-doped ZnO transparent conducting thin films for optoelectronic devices. *J. Appl. Phys.* **121**, 085302 (2017).
52. W. D. Nix, B. M. Clemens, Crystallite coalescence: A mechanism for intrinsic tensile stresses in thin films. *J. Mater. Res.* **14**, 3467–3473 (1999).
53. F. Spaepen, Interfaces and stresses in thin films. *Acta Mater.* **48**, 31–42 (2000).
54. X. Zhao, P. Munroe, D. Habibi, Z. Xie, Roles of compressive residual stress in enhancing the corrosion resistance of nano nitride composite coatings on steel. *J. Asian Ceramic Soc.* **1**, 86–94 (2013).
55. L. Dai, V. Sorkin, Y. W. Zhang, Effect of surface chemistry on the mechanisms and governing laws of friction and wear. *ACS Appl. Mater. Interfaces* **8**, 8765–8772 (2016).
56. K. L. Johnson, *Contact Mechanics* (Cambridge Univ. Press, 2012).
57. K. Holmberg, H. Ronkainen, A. Laukkanen, K. Wallin, Friction and wear of coated surfaces—Scales, modelling and simulation of tribomechanisms. *Surf. Coat. Technol.* **202**, 1034–1049 (2007).
58. K. Holmberg, H. Ronkainen, A. Laukkanen, K. Wallin, A. Erdemir, O. Eryilmaz, Tribological analysis of TiN and DLC coated contacts by 3D FEM modelling and stress simulation. *Wear* **264**, 877–884 (2008).
59. S. M. Bae, K. J. Seo, D. E. Kim, Effect of friction on the contact stress of a coated polymer gear. *Friction* **8**, 1169–1177 (2020).
60. D. Yin, Z. Xu, J. Feng, Y. Qin, Numerical modelling of multilayered coatings—Latest developments and applications. *Manufacturing Rev.* **1**, 8 (2014).
61. S. Wos, W. Koszela, P. Pawlus, The effect of both surfaces textured on improvement of tribological properties of sliding elements. *Tribol. Int.* **113**, 182–188 (2017).
62. K. P. Lijesh, M. M. Khonsari, Application of thermodynamic principles in determining the degradation of tribo-components subjected to oscillating motion in boundary and mixed lubrication regimes. *Wear* **436-437**, 203002 (2019).
63. B. J. Hamrock, S. R. Schmid, B. O. Jacobson, *Fundamentals of Fluid Film Lubrication* (CRC Press, 2004).
64. A. Kovalchenko, O. Ajayi, A. Erdemir, G. Fenske, I. Etsion, The effect of laser surface texturing on transitions in lubrication regimes during unidirectional sliding contact. *Tribol. Int.* **38**, 219–225 (2005).
65. U. Pettersson, S. Jacobson, Influence of surface texture on boundary lubricated sliding contacts. *Tribol. Int.* **36**, 857–864 (2003).
66. F. Sadeghi, Elastohydrodynamic lubrication, in *Tribology and Dynamics of Engine and Powertrain* (Elsevier, ed. 1, 2010), pp. 171–226.
67. A. Amanov, T. Watabe, R. Tsuboi, S. Sasaki, Improvement in the tribological characteristics of Si-DLC coating by laser surface texturing under oil-lubricated point contacts at various temperatures. *Surf. Coat. Technol.* **232**, 549–560 (2013).
68. S. C. Her, C. F. Chang, Effect of sputtering power on optical and electrical properties of indium tin oxide films. *Sens. Mater.* **28**, 975–981 (2016).
69. Z. W. Xie, L. P. Wang, X. F. Wang, L. Huang, Y. Lu, J. C. Yan, Influence of high temperature annealing on the structure, hardness and tribological properties of diamond-like carbon and TiAlSiCN nanocomposite coatings. *Appl. Surf. Sci.* **258**, 1206–1211 (2011).
70. R. Messier, A. P. Giri, R. A. Roy, Revised structure zone model for thin film physical structure. *J. Vac. Sci. Technol. A* **2**, 500–503 (1984).
71. S. Suematsu, K. Yatsui, T. Yano, The relationship between the hardness and the point-defect-concentration in neutron-irradiated $MgO_3.0Al_2O_3$ single crystals. *Jpn. J. Appl. Phys.* **40**, 1097 (2001).
72. A. Michalek, S. Qi, A. Batal, P. Penchev, H. Dong, T. L. See, S. Dimov, Sub-micron structuring/texturing of diamond-like carbon-coated replication masters with a femtosecond laser. *Appl. Phys. A* **126**, 144 (2020).
73. M. Taee, A. Torabi, S. Akbarzadeh, M. M. Khonsari, M. Badrossamay, On the performance of EHL contacts with textured surfaces. *Tribol. Lett.* **65**, 85 (2017).
74. C. Shen, M. M. Khonsari, Effect of dimple's internal structure on hydrodynamic lubrication. *Tribol. Lett.* **52**, 415–430 (2013).
75. R. Rahmani, I. Mirzaee, A. Shirvani, H. Shirvani, An analytical approach for analysis and optimisation of slider bearings with infinite width parallel textures. *Tribol. Int.* **43**, 1551–1565 (2010).
76. J. F. Archard, Contact and rubbing of flat surfaces. *J. Appl. Phys.* **24**, 981–988 (1953).
77. E. Martínez, J. Romero, A. Lousa, J. Esteve, Nanoindentation stress–strain curves as a method for thin-film complete mechanical characterization: Application to nanometric CrN/Cr multilayer coatings. *Appl. Phys. A* **77**, 419–426 (2003).
78. S. K. Kang, J. Y. Kim, I. Kang, D. Kwon, Effective indenter radius and frame compliance in instrumented indentation testing using a spherical indenter. *J. Mater. Res.* **24**, 2965–2973 (2009).
79. N. K. Manninen, F. Ribeiro, A. Escudeiro, T. Polcar, S. Carvalho, A. Cavaleiro, Influence of Ag content on mechanical and tribological behavior of DLC coatings. *Surf. Coat. Technol.* **232**, 440–446 (2013).
80. Y. Lin, Z. Zhou, K. Y. Li, Improved wear resistance at high contact stresses of hydrogen-free diamond-like carbon coatings by carbon/carbon multilayer architecture. *Appl. Surf. Sci.* **477**, 137–146 (2019).
81. Z. R. Liu, Y. X. Xu, B. Peng, W. Wei, L. Chen, Q. Wang, Structure and property optimization of Ni-containing AlCrSiN coatings by nano-multilayer construction. *J. Alloys Compd.* **808**, 151630 (2019).
82. O. V. Krysina, N. A. Prokopenko, Y. F. Ivanov, O. S. Tolkachev, V. V. Shugurov, E. A. Petrikova, Multi-layered gradient (Zr, Nb) N coatings deposited by the vacuum-arc method. *Surf. Coat. Technol.* **393**, 125759 (2020).
83. L. Wang, A. K. Tieu, Q. Zhu, J. Chen, J. Cheng, J. Yang, B. Kosasih, Achieving the excellent self-lubricity and low wear of TiAl intermetallics through the addition of copper coated graphite. *Compos. B. Eng.* **198**, 108223 (2020).
84. X. Sui, J. Lui, S. Zhang, J. Yang, J. Hao, Microstructure, mechanical and tribological characterization of CrN/DLC/Cr-DLC multilayer coating with improved adhesive wear resistance. *Appl. Surf. Sci.* **439**, 24–32 (2018).
85. P. E. Hovsepian, P. Mandal, A. P. Ehiasarian, G. Safran, R. Tietema, D. Doerwald, Friction and wear behaviour of Mo–W doped carbon-based coating during boundary lubricated sliding. *Appl. Surf. Sci.* **366**, 260–274 (2016).
86. D. Özkan, Y. Erarslan, E. Sulukan, L. Kara, M. A. Yilmaz, M. B. Yağci, Tribological behavior of TiAlN, AlTiN, and AlCrN coatings at boundary lubricating condition. *Tribol. Lett.* **66**, 152 (2018).
87. D. Özkan, M. A. Yilmaz, S. A. Bakdemir, E. Sulukan, Wear and friction behavior of TiB_2 thin film–coated AISI 52100 steels under the lubricated condition. *Tribol. Trans.* **63**, 1008–1019 (2020).
88. D. Özkan, Friction and wear enhancement of magnetron sputtered bilayer Cr–N/TiB_2 thin-film coatings. *Wear* **454**, 203344 (2020).
89. B. Rubig, D. Heim, C. Forsich, C. Dipolt, T. Mueller, A. Gebeshuber, R. Kullmer, R. Holecek, C. Lugmair, M. Krawinkler, V. Strobl, Tribological behavior of thick DLC coatings under lubricated conditions. *Surf. Coat. Technol.* **314**, 13–17 (2017).

Acknowledgments
Funding: This work was supported by the National Research Foundation of Korea (NRF) grant funded by the Korea government (MSIT) (no. 2020R1A2C2004714). Also, this work was supported by the National Research Foundation of Korea (NRFK) (grant no. 2020R1A2C1004784). **Author contributions:** Conceptualization, methodology, investigation, coatings deposition, experiments, analysis, visualization, FE simulation, validation, writing—original draft, and review and editing: M.K. Analysis, supervision, and writing—review and editing: O.V.P. Fabrication of micropatterns and writing—review and editing: J.J. Substrate preparation, FE simulation, and writing—review and editing: S-M.B. Coating methodology and writing—review and editing: V.S.D. Supervising the fabrication of micropatterns, writing—review and editing, and funding acquisition: B.K. Supervision, validation, writing—review and editing, and funding acquisition: D.-E.K. **Competing interests:** The authors declare that they have no competing interests. **Data and materials availability:** All data needed to evaluate the conclusions in the paper are present in the paper and/or the Supplementary Materials.

Submitted 24 June 2021
Accepted 1 October 2021
Published 19 November 2021
10.1126/sciadv.abk1224